Chemical Engineering Journal 473 (2023) 145391

Contents lists available at ScienceDirect

Chemical Engineering Journal

journal homepage: www.elsevier.com/locate/cej

Boosting redox kinetics using rationally engineered cathodic interlayers comprising porous rGO–CNT framework microspheres with $NiSe_2$-core@N-doped graphitic carbon shell nanocrystals for stable Li–S batteries

Rakesh Saroha [1], Hyun Ho Choi [1], Jung Sang Cho [*]

Department of Engineering Chemistry, Chungbuk National University, Chungbuk 361-763, Republic of Korea

ARTICLE INFO

Keywords:
Cathode materials
Multifunctional interlayers
Lithium–sulfur batteries
Metal selenide
Graphene
Carbon nanotube

ABSTRACT

Here, we propose the synthesis of a three-dimensional (3D) nanostructure comprising $NiSe_2$-core@N–doped graphitic carbon (NGC) shell nanocrystals securely implanted within a highly conductive and porous reduced graphene oxide–carbon nanotube (rGO–CNT) framework (3D P-$NiSe_2$@NGC/rGO–CNT), using spray pyrolysis technique followed by selenization and utilized as multifunctional cathodic interlayers in lithium–sulfur (Li–S) cells. The uniformly distributed arrays of macropores (ϕ = 100 nm) were formed by thermal decomposition of polystyrene nanobeads (ϕ = 200 nm). The porous structure shortens the charge diffusion length, allowing rapid charge transport and efficient electrolyte percolation besides accommodating unwanted volume perturbations. The NGC shell surrounding the $NiSe_2$ nanocrystals acted as the primary conduction conduit for electron transport, while the self-supporting rGO–CNT framework served as a secondary pathway for consecutive electron transfer besides enhancing the structural robustness. Further, the polar $NiSe_2$ nanocrystals offered numerous chemisorption sites for effectively capturing polysulfides, thus minimizing the shuttling effect and increasing active material utilization. The Li–S cell exhibited improved rate performance (till 4.0C) and excellent cycling stability (1000 cycles at 2.0C, average capacity decay rate of 0.04% per cycle). Even at severe cell parameters (effective S content = 74%, S loading = 4.5 mg cm^{-2}, and electrolyte/sulfur = 5.7 μL mg^{-1}), the cells delivered a stable rate performance and long-term cycling (400 cycles at 0.1C, average decay rate of 0.10% per cycle). We believe the nanostructure design strategy that we developed for this study could spur the development of more enduring and practical Li–S battery technology.

1. Introduction

The tremendous advances in nanostructured engineering for the various cathode or anode materials employed in commercially available lithium-ion batteries (LIBs) resulted in full utilization of their gravimetric or volumetric energy density [1–6]. However, for power grid or electric vehicle applications, new energy storage systems with higher energy density and durability are required. Among the various available alternatives, lithium–sulfur battery (LSB) technology system offers the advantages of high specific discharge capacity (1675 mA h g^{-1}), extraordinary gravimetric (2600 Wh kg^{-1}), or volumetric (2800 Wh L^{-1}) energy density [7–11], significant nominal discharge voltage (~2.1 V *vs.* Li/Li^+), natural abundance of sulfur, and low toxicity [12–17]. Despite the exceptional merits of Li–S, its commercial use has been hindered by various technical drawbacks, such as poor electronic conductivities of S (10^{-30} S cm^{-1}) and its end product (Li_2S, 10^{-13} S cm^{-1}), formation and diffusion of intermediate polysulfide species widely known as "shuttle effect" that lead to high active material loss, inferior cycling performance associated with large volume variations between S and Li_2S, and instability of Li anode causing serious battery issues [18–21]. These fundamental issues call for better cell designs and innovative nanostructured engineering at the cathode, anode, electrolyte, and even at the separator level [22–27].

Among various strategies for addressing the issues mentioned above, the use of functional separators has emerged as a promising approach. Coating interlayers not only suppresses severe shuttle effect by

* Corresponding author.
E-mail address: jscho@cbnu.ac.kr (J.S. Cho).
[1] These authors contributed equally.

https://doi.org/10.1016/j.cej.2023.145391
Received 14 June 2023; Received in revised form 7 August 2023; Accepted 10 August 2023
Available online 12 August 2023

restricting polysulfide diffusion towards the anode, but also ensures their efficient electrocatalytic conversion, thus increasing active material utilization and overall electrochemical performance [28–31]. The functional interlayers that behave as "polysulfide sieves" allow physical or chemical adsorption of intermediate lithium polysulfides (LiPS) and comprise three components: a polar material that provides enormous chemisorption sites for efficient polysulfide anchoring, a conductive matrix that facilitates rapid charge transfer during the redox processes, and finally, a porous framework that allows effective electrolyte percolation and channelizes volume variations during the redox reactions thus stabilizing the sulfur electrochemistry [13,15]. Additionally, Previously, various polar materials such as conductive porous carbons [32–35], metal sulfides [36,37], metal oxides [38–40], metal nitrides [10,25], metal phosphides [23,41], and many more [42–45] were studied as cathodic interlayers to improve the LSB performance.

Among other metal compounds, transition metal selenides (TMSes) have proved to be effective electrocatalytic materials for Li–S batteries compared to sulfides or oxides due to their better polysulfide adsorption capability, high conductivity, and significant polarity [46]. TMSes also possess lithophilic as well as sulfiphilic sites. Lithophilic sites can minimize Li dendrite formation or growth through a uniform Li^+ deposition. In contrast, the sulfiphilic sites can effectively anchor LiPS and thus prevent active material loss to a certain extent [47]. Due to the unique crystal structure and low resistivity ($\sim 10^{-3}\ \Omega$ cm) of $NiSe_2$, it has become a favored material in electrocatalytic applications [48]. The abundant and accessible active sites in $NiSe_2$ are believed to be useful as robust polysulfide anchors, although their high conductivity could shorten the nucleation path of Li_2S.

To further enhance the overall conductivity, the $NiSe_2$ nanocrystals were well-embedded inside the 3D reduced graphene oxide and carbon nanotubes (rGO–CNT) framework, apart from the surrounding N-doped graphitic carbon (NGC) shell. The NGC shell acts as a primary electron pathway to facilitate fast and continuous electron transfer. In contrast, the self-supporting rGO–CNT framework serves as a secondary pathway for the subsequent electron transfer during the electrochemical process. Moreover, rGO–CNT stabilizes the 3D porous matrix as CNTs perform bridging between the rGO nanosheets and prevent them from falling apart. The porosity inside the 3D conductive matrix was introduced using polystyrene (PS) nanobeads-based suspension (ϕ = 200 nm) as porogen. The porous structure offers smooth diffusion of charged species by shortening the effective charge diffusion length and lowering the overall electrolyte volume consumption inside the cell, which helps to reduce a key Li–S cell parameter (electrolyte/sulfur, E/S) to more realistic values. The highly porous structure is also better for confining more polysulfide or sulfur-like species within the cathodic domain and channeling the severe volume variations during the lithiation/delithiation processes.

Based on the above discussion, we introduced a rationally-engineered cathodic interlayer comprising a 3D porous and conductive framework with well-embedded NGC shell nanocrystals in an rGO–CNT framework (abbreviated as "3D P-$NiSe_2$@NGC/rGO–CNT") as polysulfide sieves to improve LSB performance. We used a facile spray pyrolysis method to construct the hierarchical 3D porous nanostructure with highly conductive pathways (in the form of an NGC shell and rGO–CNT framework) and robust structural integrity. The subsequent selenization process formed well-embedded $NiSe_2$ nanocrystals that promote the fast electrocatalytic conversion of LiPS. Correspondingly, the Li–S cells featuring porous, conductive, electrocatalytic, and adsorptive barrier in the form of 3D P-$NiSe_2$@NGC/rGO–CNT microspheres exhibited overall enhanced sulfur redox kinetics. For instance, the Li–S cells paired with 3D P-$NiSe_2$@NGC/rGO–CNT-coated separator and regular S electrode (effective S content = 60.4%) displayed high-rate capability (till 4.0C) and excellent cycling performance at low (500cycles at 0.5C), as well as high C-rate (1000 cycles at 2.0C, 0.04% decay rate per cycle). Even with more practical parameters (effective S content = 74%, S-loading = 4.5 mg cm^{-2}, and E/S = 5.7 μL mg^{-1}), the Li–S cells exhibited excellent rate (till 0.3C) and cycling performance (400 cycles at 0.1C). Therefore, we anticipate that the structural merits presented in this work will pioneer new insights in pursuit of more durable sulfur redox kinetics for a wide range of practical applications.

2. Results and discussion

2.1. Physical characterization of as-prepared powders

Scheme 1 shows the detailed synthesis involving the formation of 3D porous and highly conductive microspheres comprising well-embedded $NiSe_2$-core@N–doped graphitic carbon (NGC) shell nanocrystals inside the reduced graphene oxide–carbon nanotube framework (abbreviated as 3D P-$NiSe_2$@NGC/rGO–CNT microspheres) *via* facile spray pyrolysis (Scheme S1) followed by selenization under a reducing atmosphere (5% H_2/Ar). Scheme 1a-① shows the aqueous droplets formed by an ultrasonic nebulizer comprising uniformly dispersed Ni-salt, PVP as carbon source, PS nanobeads suspension (ϕ = 200 nm), GO nanosheets, and CNT. The droplets were allowed to pass through a vertically oriented quartz tube preheated at 700 ℃ with flowing N_2 as carrier gas. The resulting drying process reduced the droplets to a more compact form. In addition, the Ni-salt transformed to a metallic-Ni phase, while the PVP decomposed to the C-matrix (Scheme 1a-②). The complete thermal breakdown of the PS nanobeads led to the formation of macropores uniformly distributed throughout the microsphere (Scheme 1a-③). Moreover, the C-matrix around Ni-nanocrystals consecutively transformed to the more uniform NGC shell due to the catalytic effect of the metallic-Ni, which forms a Ni-core@NGC shell. The NGC shell acted as the primary transport pathway that guaranteed fast and uninterrupted passage for electrons (Scheme 1b-①, ②), which were consecutively transported to the secondary pathways consisting of rGO–CNT framework (Scheme 1b-③). The as-sprayed powders were then subjected to a selenization process at 400 ℃ for 3 h at a ramp rate of 5 ℃ min^{-1} under a reducing atmosphere (5% H_2/Ar). The excess selenium powder was used to form H_2Se gas. During the selenization, the metallic-Ni nanocrystals converted to the NGC-coated $NiSe_2$ nanocrystals and embedded inside the rGO–CNT conductive framework (Scheme 1a-④). Similarly, 3D porous microspheres comprising $NiSe_2$ nanocrystals well-wrapped inside the PVP-derived NGC-skeleton (i.e., without an rGO–CNT framework) were also prepared using an identical process (abbreviated as 3D P-$NiSe_2$@NGC) for comparison purpose. A non-porous or filled sample (i.e., without PS nanobeads) that also does not contain any conductive framework (i.e., rGO and CNT) was also prepared as a standard (abbreviated as F-$NiSe_2$@NGC, where 'F' indicates filled structure).

The synthesis of the 3D P-$NiSe_2$@NGC/rGO–CNT microspheres was validated through morphological and crystal structural characterization techniques of the powders obtained after each synthesis step. Fig. 1 shows the physical characteristics of 3D porous microspheres comprising well-embedded NGC shell nanocrystals in the rGO–CNT framework (3D P-metallic-Ni@NGC/rGO–CNT) obtained after spray pyrolysis. The FE-SEM micrographs in Fig. 1a and 1b suggest the formation of non-aggregated spherical-shaped microspheres with a mean diameter of approximately 1.3 μm. Also, the presence of macropores (average diameter of approximately 100 nm) all over the external surface of the microspheres was apparent. The fractured FE-SEM image in Fig. 1c also revealed a porous structure corresponding to macropores. The macropores were formed due to the thermal decomposition of the PS nanobeads (ϕ = 200 nm) during spray pyrolysis. However, the decrease in pore diameter from 200 to 100 nm was primarily due to microsphere shrinkage during the pyrolysis. The TEM image in Fig. 1d, which shows the formation of homogeneously dispersed 3D spherically-shaped microspheres (average diameter = 1.3 μm), is consistent with those taken with the FE-SEM. The amplified TEM image in Fig. 1e indicated the presence of ordered macropore arrays (highlighted by arrows) surrounded by carbon walls (C-walls). A C-wall was primarily

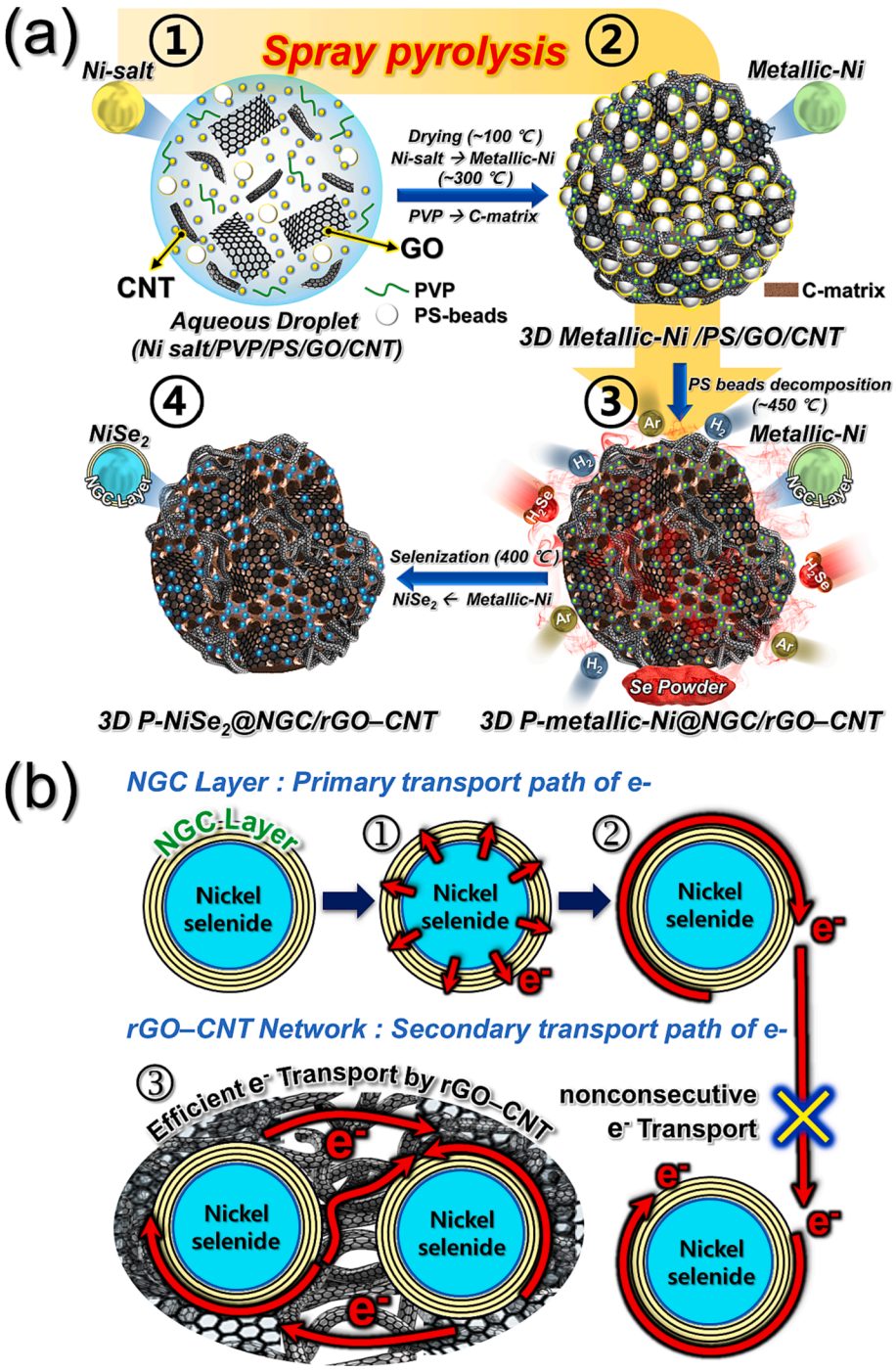

Scheme 1. (a) Schematic representation of the formation mechanism of 3D P-$NiSe_2$@NGC/rGO–CNT microspheres *via* facile spray pyrolysis technique and subsequent selenization and (b) efficient transport pathways for electrons by NGC shell and rGO–CNT framework during the electrochemical processes.

composed of an rGO–CNT framework (highlighted by arrows), as indicated in Fig. 1f. Here, the rGO–CNT framework enhanced the structural integrity and increased the electrical conductivity of the microspheres. Entangled CNTs in the nanostructure ensured a smooth and continuous flow of charge carriers in vertical and longitudinal directions. Moreover, the high-resolution TEM (HR-TEM) image in Fig. 1g shows uniformly dispersed metallic-Ni nanocrystals embedded inside a carbonaceous framework. The average metallic-Ni nanoparticle size was approximately 6 nm. The PVP-derived carbon around Ni nanocrystals transformed into the NGC shell (highlighted by arrows) due to the catalytic effect of the metallic-Ni nanocrystals. Fig. 1g (right panel) also confirmed the presence of CNT (highlighted by arrows), as well as crystal lattice fringes with a separation of 0.20 nm, corresponding to the (1 1 1) crystal plane of the metallic-Ni nanocrystals. Fig. 1h and 1i show the selected area electron diffraction (SAED) and XRD patterns, respectively, in which the clear diffraction rings were attributed only to the metallic Ni and NGC framework. These results were consistent with those inferred from the TEM images. The elemental dot mapping images shown in Fig. 1j also suggest the presence of metallic-Ni@NGC nanocrystals embedded inside the rGO–CNT-derived carbonaceous framework. The N in the mapping images originated from the nitrogen-rich units in the PVP polymer.

The as-sprayed 3D P-metallic-Ni@NGC/rGO–CNT microspheres were subjected to a selenization process at 400 ℃ for 3 h under a

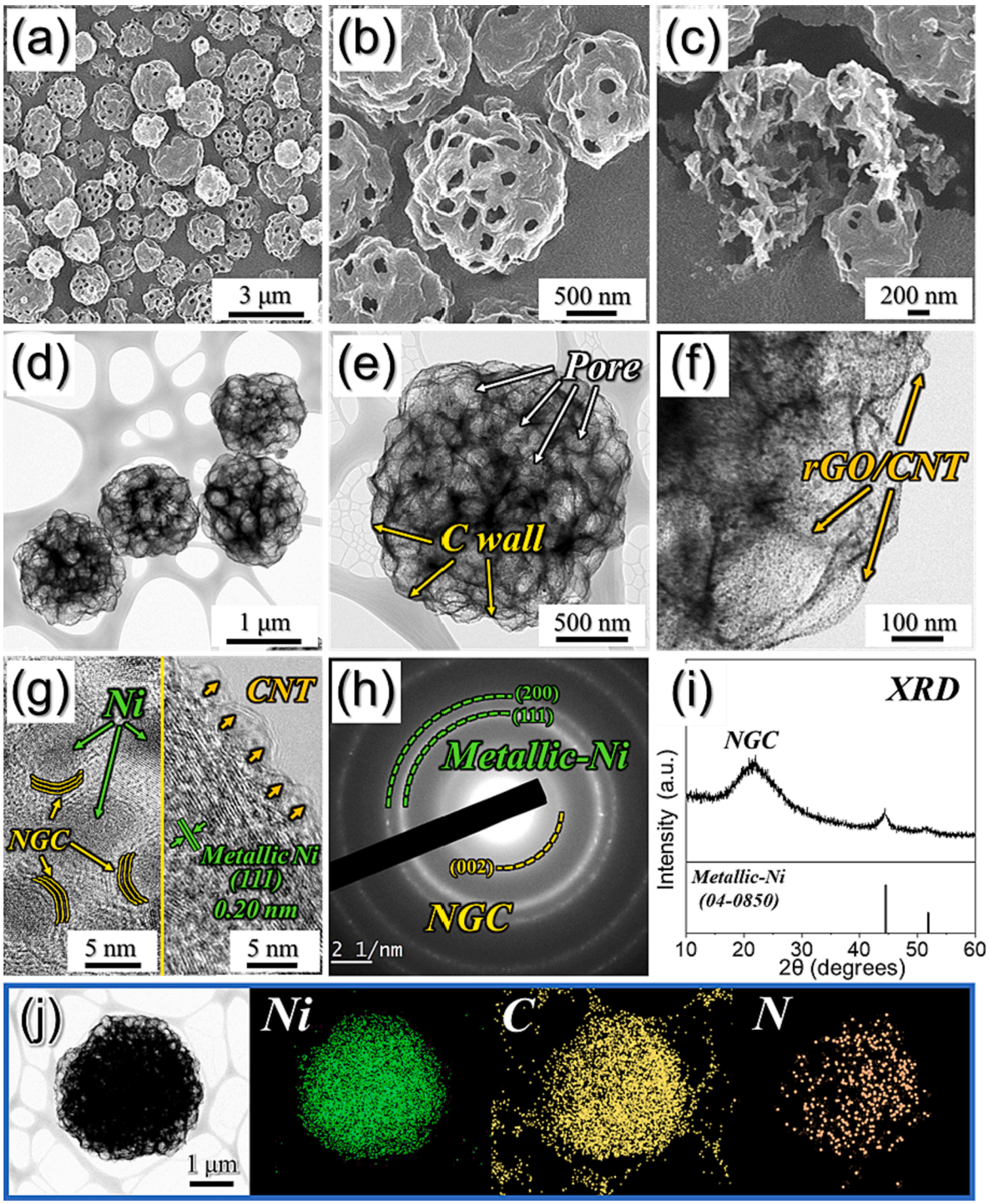

Fig. 1. Physical characterizations of 3D P-metallic-Ni@NGC/rGO–CNT microspheres obtained after spray pyrolysis: (a, b) FE-SEM images, (c) Fractured FE-SEM image, (d-f) TEM images, (g) HR-TEM image, (h) SAED pattern, (i) XRD pattern, and (j) Elemental dot mapping images.

reducing atmosphere (5% H_2/Ar). Fig. 2 shows the morphological and phase changes in the 3D P-$NiSe_2$@NGC/rGO–CNT microspheres obtained after selenization. The FE-SEM micrograph in Fig. 2a strongly indicates that the 3D spherical morphology was maintained with an average microsphere diameter of about 1.2 μm. The porous structure shown in Fig. 2b also remained intact as inferred from the absence of any deformation, suggesting the structural robustness of the prepared powders. Moreover, the cross-sectional image shown in Fig. 2c also confirms the porous structure. The TEM images in Fig. 2d and 2e were consistent with the FE-SEM results. However, the grain growth and crystallization process of metallic Ni during the heat treatment resulted in the formation of slightly larger nanocrystals. The high-magnification TEM image in Fig. 2f also indicates the presence of $NiSe_2$ nanocrystals encapsulated by the rGO–CNT framework (highlighted by arrows). The average $NiSe_2$ nanocrystal size was approximately 50 nm. The HR-TEM image in Fig. 2g clearly indicates the presence of $NiSe_2$ nanocrystals well-grafted within the rGO–CNT framework. The clear lattice fringes with a 0.26-nm separation corresponding to the (2 1 0) crystal plane of $NiSe_2$ were also observed. The SAED pattern in Fig. 2h reveals diffraction rings corresponding to the $NiSe_2$ cubic phase and PVP-derived NGC

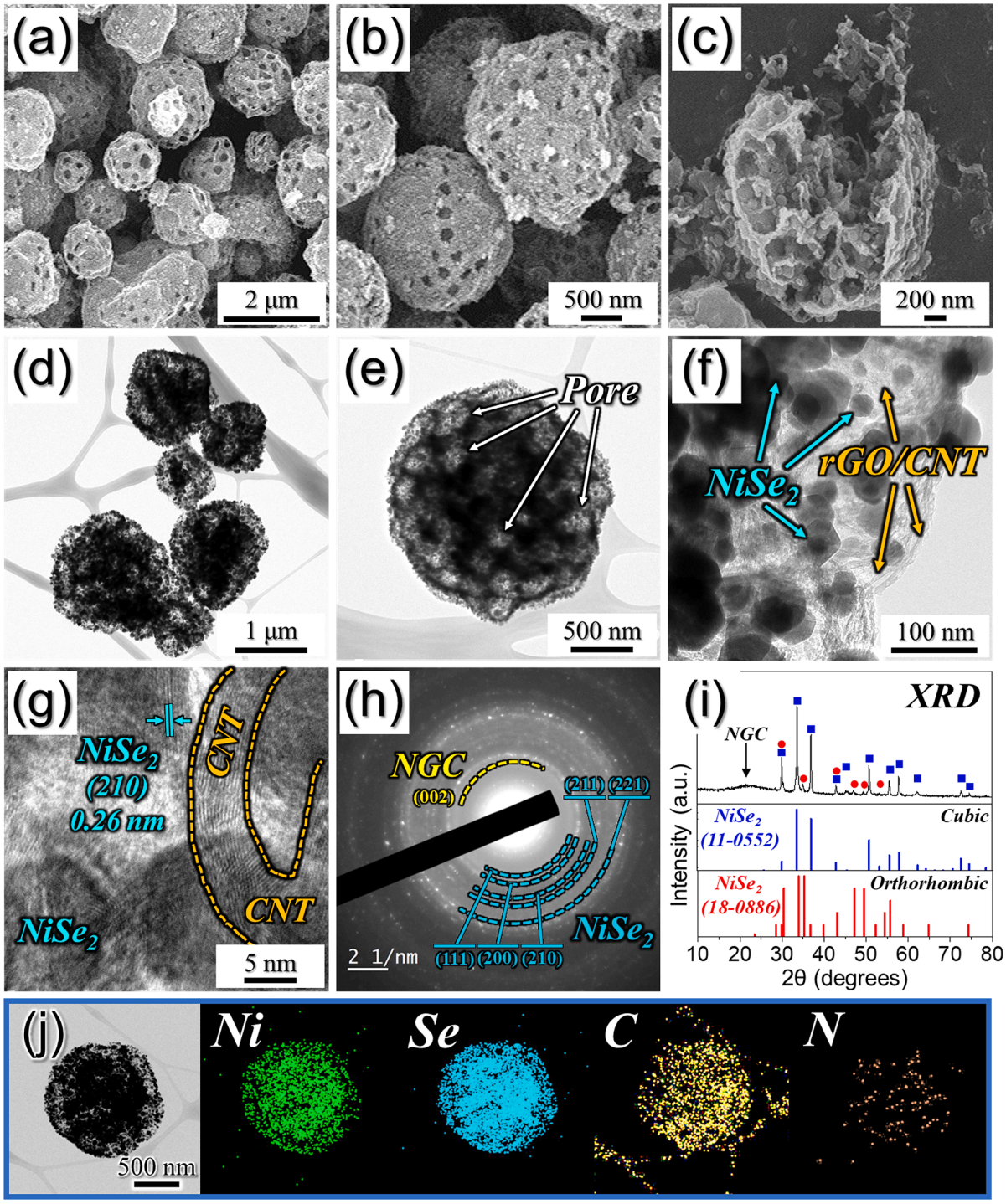

Fig. 2. Physical characterizations of 3D P-$NiSe_2$@NGC/rGO–CNT microspheres obtained after selenization at 400 ℃ for 3 h: (a, b) FE-SEM images, (c) Fractured FE-SEM image, (d-f) TEM images, (g) HR-TEM image, (h) SAED pattern, (i) XRD pattern, and (j) Elemental dot mapping images.

framework. The XRD pattern in Fig. 2i suggests a few low-intensity peaks corresponding to the orthorhombic phase of $NiSe_2$. However, the cubic phase appeared more dominant with well-distinguished sharp and intense peaks. Besides, the average crystallite size was also calculated using the Scherrer equation by considering the highest intensity peak and comes out to be 90 nm. The elemental dot mapping images in Fig. 2j indicate the formation of phase-pure $NiSe_2$ with homogenous Ni, Se, C, and N distribution throughout the microspheres. Overall, the above results validate the formation of 3D porous and highly conductive microspheres comprising NGC shell nanocrystals encapsulated by the rGO–CNT framework.

Using XPS, we examined the chemical environment and bonding states of various elements in 3D P-$NiSe_2$@NGC/rGO–CNT microspheres. The survey spectrum in Fig. S1 indicates the presence of photoelectron signals corresponding to the Ni 2*p*, O 1*s*, N 1*s*, C 1*s*, and Se 3*d* orbital states. The high-resolution Ni 2*p* XPS spectrum (Fig. 3a) shows well-resolved peaks for Ni $2p_{3/2}$ and Ni $2p_{1/2}$ flanked by respective satellite peaks (marked "*Sat.*") [21,49,50]. Furthermore, the deconvolution spectra revealed that the peak centered at 852.4 eV for Ni $2p_{3/2}$ and 869.7 eV for Ni $2p_{1/2}$ was due to Ni^{2+} [51]. Likewise, the peak centered

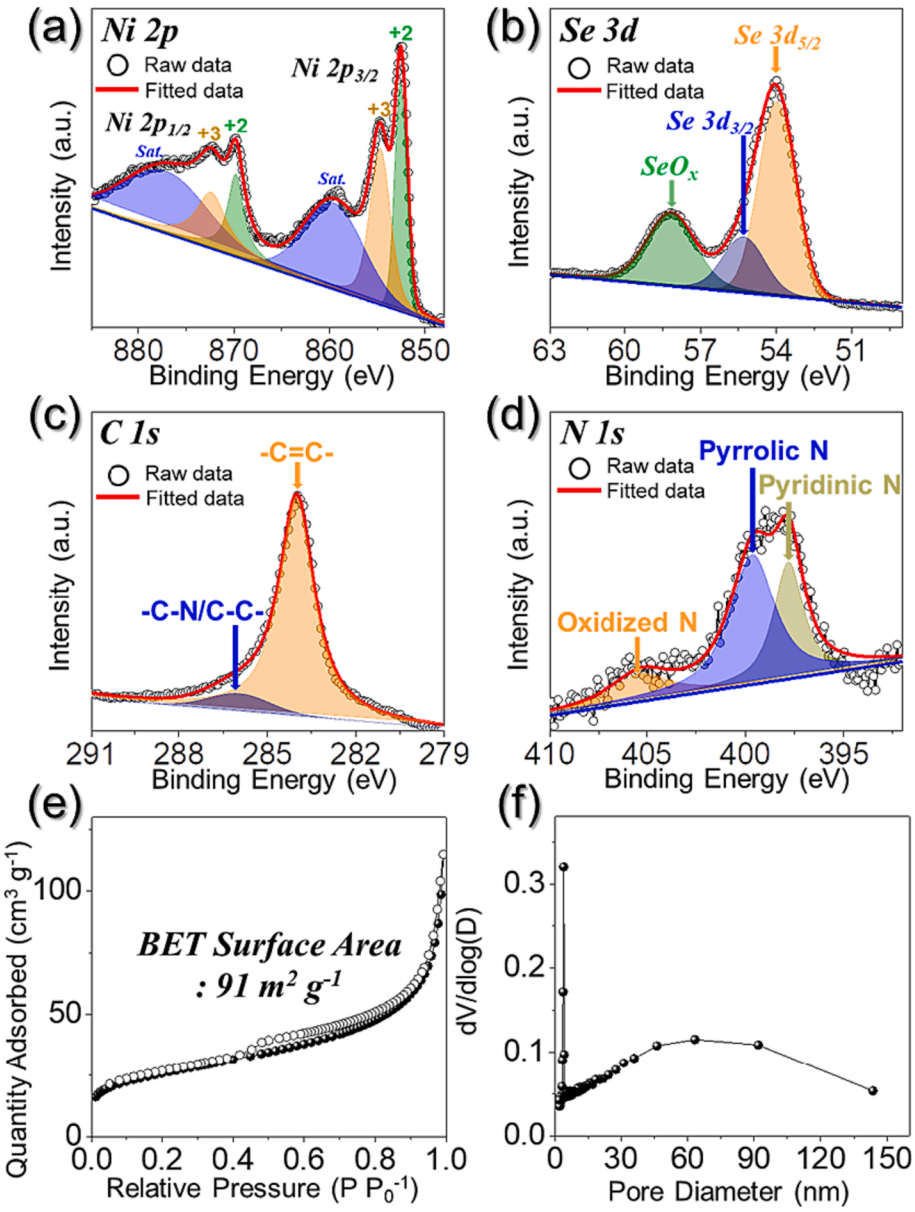

Fig. 3. XPS characterizations of 3D P-$NiSe_2$@NGC/rGO–CNT microspheres obtained after selenization at 400 ℃ for 3 h: (a) Ni 2*p* XPS spectrum, (b) Se 3*d* XPS spectrum, (c) C 1*s* XPS spectrum, (d) N 1*s* XPS spectrum, (e) N_2 adsorption–desorption isotherms, and (f) BJH desorption pore-size distribution.

at 854.6 eV for Ni $2p_{3/2}$ and 872.4 eV for Ni $2p_{1/2}$ was assigned to Ni^{3+} [52]. The Se 3*d* XPS spectrum in Fig. 3b exhibited closely-spaced photoelectron peaks for Se $3d_{5/2}$ (binding energy = 53.9 eV) and Se $3d_{3/2}$ (binding energy = 55.3 eV), which could be assigned to the interaction of Se with metallic-Ni in $NiSe_2$ [53,54]. The peak at 58.1 eV corresponded to the surface oxidation of the Se (Se–O bond) under atmospheric conditions, consistent with previous reports [55]. The deconvoluted C 1*s* spectrum in Fig. 3c displays two well-resolved peaks corresponding to the -C = C- (283.9 eV) and -C–N/C–C- (286.0 eV) bonding species [56]. Moreover, the high intensity of the -C = C- peak clearly indicates the existence of a carbonaceous framework (rGO–CNT) in the prepared microspheres [57,58]. Additionally, the -C–N/C–C- peak implies N-doping in the carbon framework, which enhanced the electronic conductivity of the microspheres due to the N-atom's high electronegativity compared to the C-atom [59]. We analyzed the N 1*s* deconvoluted spectrum to verify the above results (Fig. 3d). The spectrum exhibits three well-fitted peaks corresponding to the pyridinic N (397.7 eV), pyrrolic N (399.6 eV), and oxidized N (405.3 eV), consistent with N-doping in the carbonaceous framework [10,60]. We also conducted elemental analysis (EA) to validate our XPS data (see summary in Table S1). The N content was estimated to be 1.2 wt%, thus confirming the presence of an N-doped carbon matrix. The PVP polymer's N-rich organic units induced the N-doping in the nanostructure. Fig. S2a shows the TG curve we obtained in an air atmosphere to quantify the carbon content in 3D P-$NiSe_2$@NGC/rGO–CNT microspheres. The carbon content was estimated to be around ~ 15 wt% (see supporting information) and fairly matched the EA results in Table S1. Fig. S3 shows the Raman spectrum obtained to determine the crystalline nature of the carbonaceous species in the microspheres. The spectrum exhibits three well-resolved peaks at 509, 1340, and 1572 cm^{-1} corresponding to the Ni–Se bond, D-, and G-bands, respectively, in the nanostructure [53,61]. The relative intensity ratio of the D- and G-bands (i.e., I_D/I_G) measures the crystalline nature of the carbonaceous species in the prepared microspheres [62]. An I_D/I_G value of 1.0 indicates crystalline carbonaceous products. N_2 adsorption–desorption isotherms were plotted to analyze the surface area and pore size distribution of 3D P-$NiSe_2$@NGC/rGO–CNT microspheres. As shown in Fig. 3e, the sample exhibited a high surface area of 91 $m^2\ g^{-1}$ primarily due to the PS

nanobeads-derived macropores uniformly distributed in the microspheres. The pore size distribution curve in Fig. 3f also indicates a broad peak at 65 nm, confirming the presence of macropores. The sharp peak at 3.5 nm was due to the tensile strength effect of N_2 adsorption, as reported previously [56]. Macropores in the nanostructure provide enough space to absorb the unwanted volume fluctuations besides facilitating efficient electrolyte percolation along with the fast diffusion of charged species.

The structural merits in 3D P-$NiSe_2$@NGC/rGO–CNT microspheres were further verified using a comparison sample synthesized using a spray solution that consisted of Ni-salt, PVP, and PS nanobeads in deionized water (i.e., without rGO and CNT). The physical properties of the as-sprayed sample are shown in Fig. S4. The FE-SEM micrographs in Fig. S4a and S4b suggested the formation of 3D porous microspheres (average diameter of ~ 1.0 μm) with uniformly distributed macropores all over the microsphere surface. The presence of ordered arrays of macropores (mean diameter of 80 nm) was apparent in the high-magnification FE-SEM micrograph (Fig. S4b and S4c). However, the size of pores decreased significantly from 200 nm to 80 nm due to shrinkage of the microspheres during spray pyrolysis. The XRD pattern

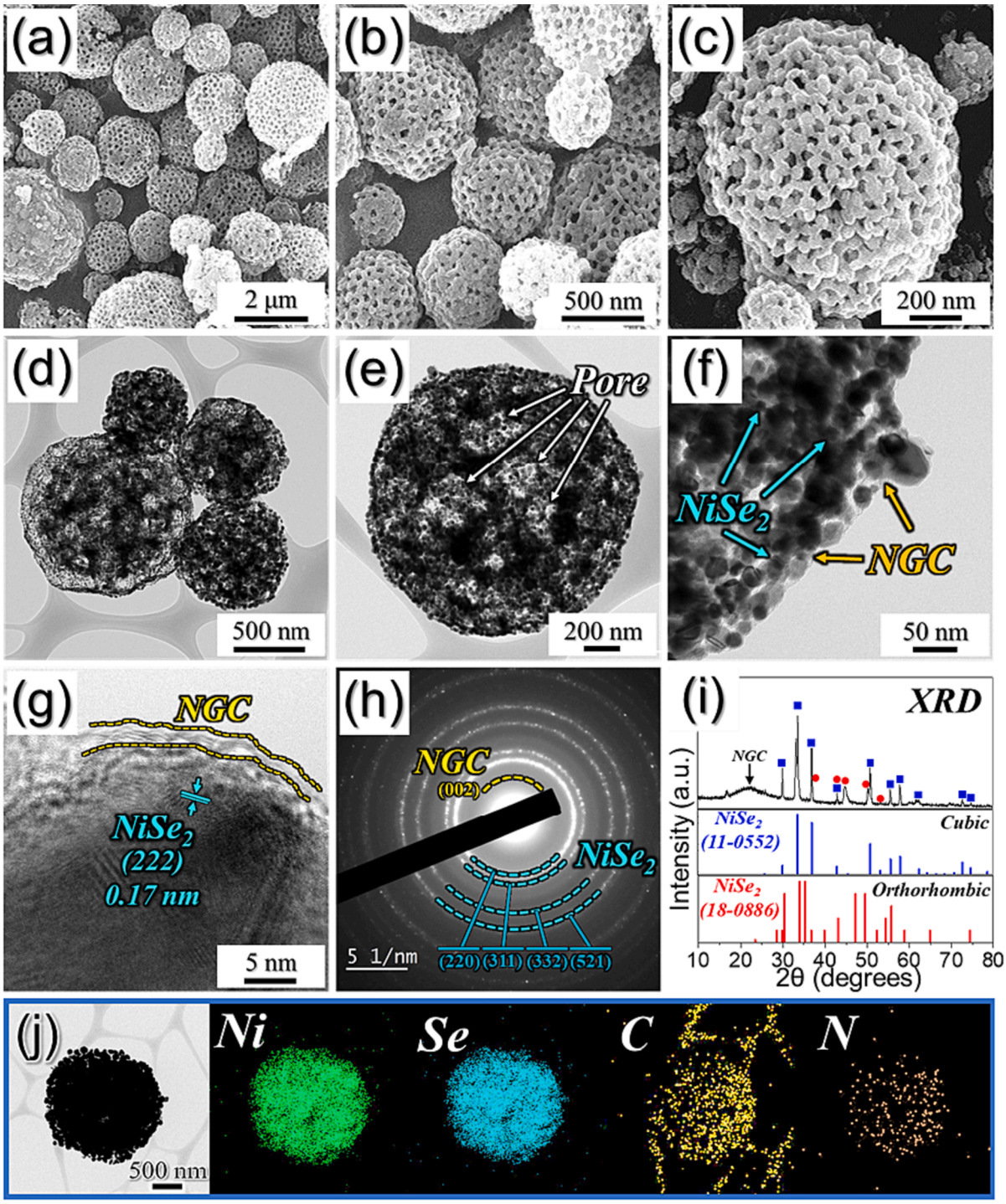

Fig. 4. Physical characterization of 3D P-$NiSe_2$@NGC microspheres obtained after selenization at 400 ℃ for 3 h: (a-c) FE-SEM images, (d-f) TEM images, (g) HR-TEM image, (h) SAED pattern, (i) XRD pattern, and (j) Elemental dot mapping images.

in Fig. S4d indicated the existence of metallic Ni as the dominant phase flanked by a few low-intensity peaks corresponding to the NiO phase. A broad peak at $2\theta = 21.4^{\circ}$ was due to the PVP-derived NGC skeleton. The as-sprayed microspheres were further subjected to the selenization process at 400 ℃ for 3 h under a reducing atmosphere (5% H_2/Ar) to obtain 3D P-$NiSe_2$@NGC microspheres. The morphological and phase changes of the obtained microspheres after selenization are presented in Fig. 4. The FE-SEM micrograph in Fig. 4a revealed that the 3D porous nature of microspheres (with a mean diameter of ~ 1.0 μm) remained intact even after the selenization process. In addition, the high-magnification FE-SEM images in Fig. 4b and 4c suggested that the PS nanobeads-derived macropores arrays were also present. However, closer examination revealed the uncontrolled growth and crystallization of the metallic-Ni nanocrystals. This is primarily due to the absence of an rGO–CNT framework that restricted grain growth during the selenization process and thus minimized agglomeration. The TEM images in Fig. 4d and 4e shows uniformly dispersed 3D porous microspheres with well-rooted macropores throughout the nanostructure confirmed our FE-SEM results. The high-magnification TEM image in Fig. 4f also revealed the presence of tightly packed $NiSe_2$ nanocrystals in the NGC skeleton. The HR-TEM image in Fig. 4g shows an NGC shell and well-resolved lattice fringes separated by 0.17 nm corresponding to the (222) crystal plane of the $NiSe_2$. The SAED pattern in Fig. 4h suggested well-resolved diffraction rings corresponding to the NGC and $NiSe_2$ phases only. Likewise, the XRD pattern in Fig. 4i displays sharp, intense peaks corresponding to the cubic phase and limited low-intensity diffraction peaks attributed to the orthorhombic phase. The elemental dot mapping images in Fig. 4j indicate the formation of $NiSe_2$ with a uniform dispersion of elements such as Ni, Se, C, and N. The percentage of carbon and nitrogen element in 3D P-$NiSe_2$@NGC microspheres is presented in Table S1, indicating the presence of nitrogen-doped carbonaceous species in the form of NGC only. Furthermore, a low Brunauer–Emmett–Teller surface area (Fig. S5a) of 18 $m^2\ g^{-1}$ confirmed that the uncontrolled growth and crystallization of $NiSe_2$ nanocrystals during selenization filled a large portion of the available space in the microspheres. The pore size distribution curve in Fig. S5b was consistent

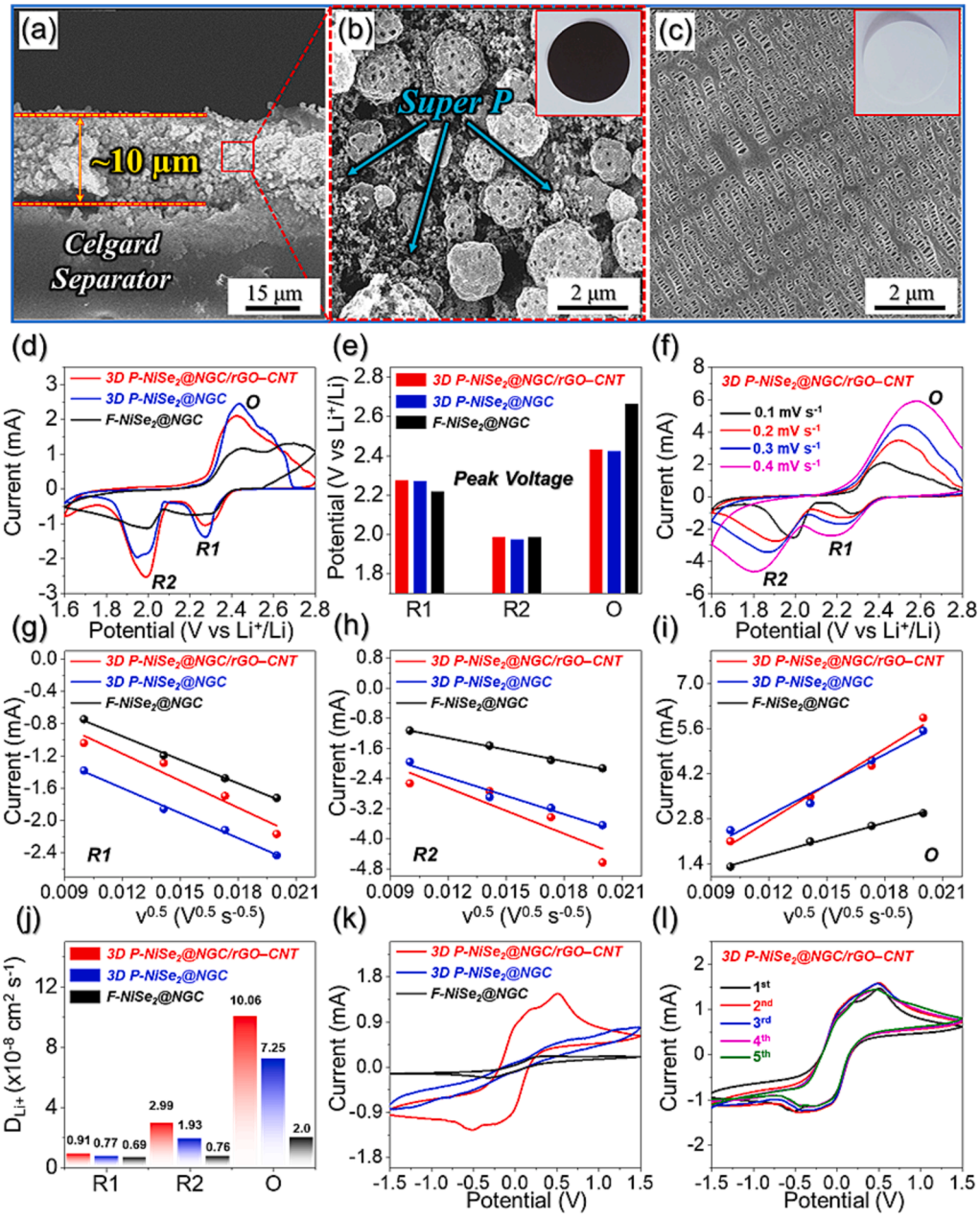

Fig. 5. (a) Cross-sectional FE-SEM image of 3D P-$NiSe_2$@NGC/rGO–CNT-coated separator, (b) Magnified view of the coated separator, (c) FE-SEM image of the pristine separator, (d) CV profiles of Li–S cells featuring different coated separator arrangements at 0.1 mV s^{-1}, (e) Redox peak voltage comparison obtained from CV graphs, (f) CV profile at various voltage scan rates, (g-i) Peak current versus square root of the voltage scan rate plots for reduction and oxidation peaks, (j) Lithium-ion diffusion coefficient (D_{Li}^{+}) values comparison, (k) Comparison of electrocatalytic activity of as-prepared nanostructures using CV profiles from symmetric cells at a scan rate of 1.0 mV s^{-1}, and (l) Five initial CV scans for symmetric cell featuring 3D P-$NiSe_2$@NGC/rGO–CNT microspheres as counter and working electrode.

with the above results and again confirmed the existence of macropores. Another control sample (named "F-$NiSe_2$@NGC") consisting only of Ni-salt and PVP (i.e., without rGO, CNT, and PS nanobeads) in deionized water as spray solution was also prepared under identical conditions. The various physical and morphological characteristics of the as-sprayed and post-selenized samples are presented in Fig. S6 and Fig. S7, respectively.

2.2. Electrochemical performance of the prepared nanostructures

The rationally designed porous and highly conductive microspheres were utilized as cathodic interlayers by coating the samples on a commercial Celgard separator facing the conventional sulfur electrodes. The cross-sectional FE-SEM image of the coated separator in Fig. 5a indicates a coating thickness of ~ 10 μm. Furthermore, a magnified FE-SEM image in Fig. 5b shows a uniform coating of 3D P-$NiSe_2$@NGC/rGO–CNT microspheres and super-P over the separator surface. In particular, the coating was homogeneous and crack-free, as revealed from the digital image of the coated separator in the inset of Fig. 5b. The FE-SEM micrograph of the pristine Celgard separator in Fig. 5c indicates submicron openings that could allow the diffusion of charged species and electrolytes during an electrochemical process. The prepared multifunctional interlayers, regular sulfur electrodes, and metallic-Li as anode were utilized in CR2032-type coin cells to evaluate electrochemical performance improvement. Based on the coated separator loading, the effective sulfur content in the cathode region was approximately 60.4%. The Li–S cells utilizing 3D P-$NiSe_2$@NGC/rGO-CNT, 3D P-$NiSe_2$@NGC, and F-$NiSe_2$@NGC microspheres as coated separators were subjected to CV tests, as shown in Fig. 5d. During the initial cathodic scan at 0.1 mV s^{-1}, all the cells exhibited a typical two-step sulfur reduction process. The reduction peak denoted "R1" suggested the reduction of elemental sulfur to a highly soluble, higher or middle-order LiPS (Li_2S_x, $4 \leq x \leq 8$). In contrast, the reduction peak marked "R2" was associated with a further reduction to an insoluble solid Li_2S_2/Li_2S state [63]. During the anodic scan, the peak marked as "O" indicated a single-step oxidation of Li_2S_2/Li_2S to elemental sulfur *via* Li_2S_x [15]. For the F-$NiSe_2$@NGC-coated separator, the two well-distinguished broad oxidation peaks suggested a two-stage oxidation process. Furthermore, the cell with a 3D P-$NiSe_2$@NGC/rGO–CNT-coated separator exhibited sharp and intense redox peaks, indicating improved redox kinetics and better active material utilization. This observation became more apparent if one considered the individual redox peak voltage values and their respective polarization, as shown in Fig. 5e. The cell with the 3D P-$NiSe_2$@NGC/rGO–CNT exhibited the lowest polarization potential ($\Delta V = 159$ mV) compared to the cells coated with 3D P-$NiSe_2$@NGC ($\Delta V = 169$ mV) and F-$NiSe_2$@NGC ($\Delta V = 448$ mV) separators. The four initial CV cycles in Fig. S8 indicated substantially-overlapping profiles suggesting highly reversible and kinetically-favored redox processes inside the cells. To prove the better redox kinetics inside the Li–S cell with a 3D P-$NiSe_2$@NGC/rGO-CNT-coated separator compared to those occurring in the other cells, the CV curves at different voltage scan rates ranging from 0.1 – 0.4 mV s^{-1} are measured and analyzed, as shown in Fig. 5f. The shape of the CV curves strongly indicated that the redox processes involved S and Li_2S only and exhibited typical redox signatures even at high voltage scan rates. However, the current intensity increased with more voltage hysteresis at high scan rates. Likewise, the CV curves for the Li–S cells with 3D P-$NiSe_2$@NGC and F-$NiSe_2$@NGC-coated separators in Fig. S9 showed similar redox characteristics. However, the current intensity and voltage hysteresis differed in those systems, suggesting that the extent of redox reactions was not identical. The diffusion kinetics inside the cells was evaluated using the well-known Randles–Sevcik equation [23]:

$$I_p = 2.69 \times 10^5 n^{1.5} A\, D_{Li^+}^{0.5}\, C_{Li}\, \nu^{0.5} \quad (1)$$

where the variables carry the usual meanings. The Li-ion diffusion coefficient (D_{Li}^{+}) was calculated for all Li–S cells using the slope from I_p versus $\nu^{0.5}$ curves for the three redox peaks (i.e., R1, R2, and O), as shown in Fig. 5g–5i. The obtained D_{Li}^{+} values are summarized in Fig. 5j. The highest D_{Li}^{+} values for all three peaks suggest improved reaction kinetics inside the Li–S cell with the 3D P-$NiSe_2$@NGC/rGO–CNT-coated separator compared to the 3D P-$NiSe_2$@NGC and F-$NiSe_2$@NGC-coated interlayers. This was primarily attributed to the robust nanostructure engineering methodology that favored structural integrity and guaranteed the synergetic effects between various components. For instance, the NGC coating surrounding the $NiSe_2$ nanocrystals acted as a primary electron pathway for facilitating fast electron transfer to support a smooth catalytic conversion of trapped polysulfide species. In contrast, the self-supporting rGO–CNT framework (in which entangled CNTs connected the graphene nanosheets and allowed longitudinal and vertical electron transport) served as secondary pathways for consecutive electron transfer during the electrochemical process (Scheme S2). Additionally, the well-grafted $NiSe_2$ nanocrystals functioned as active chemisorption sites for efficient anchoring and electrocatalytic conversion of the trapped polysulfide species, thus ensuring high active material utilization. The above results were further verified by examining the symmetric cell configurations to determine the extent of the electrocatalytic conversion effect of all the prepared nanostructures. The initial CV curve within the voltage window of –1.5 to 1.5 V (Fig. 5k) strongly indicated that the symmetric cell with 3D P-$NiSe_2$@NGC/rGO–CNT microspheres acting as both counter and working electrode exhibits well-distinguished and symmetric peaks pair at –0.52 V and 0.51 V. The peak at –0.52 V corresponds to the decomposition of Li_2S_6 to Li_2S, whereas the symmetric peak at 0.51 V represents the reverse process, explaining effective electrocatalytic behavior towards LiPS. In contrast, the 3D P-$NiSe_2$@NGC and F-$NiSe_2$@NGC symmetric cells displayed weak electrocatalytic characteristics towards LiPS. Also, the five consecutive CV cycles in Fig. 5l almost overlapped, indicating the repeated catalytic conversion capability of the 3D P-$NiSe_2$@NGC/rGO–CNT microspheres. Overall, the above results demonstrated enhanced electrochemical performance for the 3D P-$NiSe_2$@NGC/rGO–CNT microspheres compared to the 3D P-$NiSe_2$@NGC and F-$NiSe_2$@NGC microspheres due to the robust structure, porous framework, highly conductive skeleton, and polar chemisorption sites.

Based on the above results, we performed further electrochemical characterizations to confirm the enhancement in redox processes derived from structural merits. Fig. 6a reveals the initial galvanostatic charge–discharge (GCD) voltage profile at 0.1C for different coated separator arrangements. The profiles exhibited two discharge voltage plateaus and a slopping charging profile revealing multistep sulfur redox processes, which were well synchronized with the CV curves in Fig. 5d. However, the length of redox voltage plateaus was also different for all arrangements suggesting uneven redox kinetics inside the cells. Among all the assembled Li–S cells, the cell with the 3D P-$NiSe_2$@NGC/rGO–CNT-coated separator displayed the longest redox voltage plateaus length and lowest voltage polarization (denoted as "ΔE") measured between the second reduction and oxidation voltage plateau. The calculated ΔE values are summarized in Fig. 6b. These calculated values suggested that the 3D P-$NiSe_2$@NGC/rGO–CNT-coated separator exhibited lower polarization value ($\Delta E = 180$ mV) than 3D P-$NiSe_2$@NGC ($\Delta E = 222$ mV) and F-$NiSe_2$@NGC ($\Delta E = 311$ mV). Furthermore, two independent variables, Q1 and Q2, and their relative ratio (i.e., Q2/Q1) were also measured. The Q1, measured as the discharge capacity value (theoretical value = 419 mA h g^{-1}) exhibited by the first discharge plateau and sloppy region, is related to the amount of LiPS formation and their diffusion towards the anode. Likewise, the Q2 measured as the discharge capacity value (theoretical value = 1256 mA h g^{-1}) exhibited by the second discharge plateau and subsequent sloppy region is associated with the efficient conversion of LiPS to Li_2S [64]. Therefore, the Q2/Q1 ratio (theoretical value = 3) represents the electrocatalytic conversion capability of the prepared nanostructure [65]. Higher Q2/Q1 guarantees better catalytic conversion of the

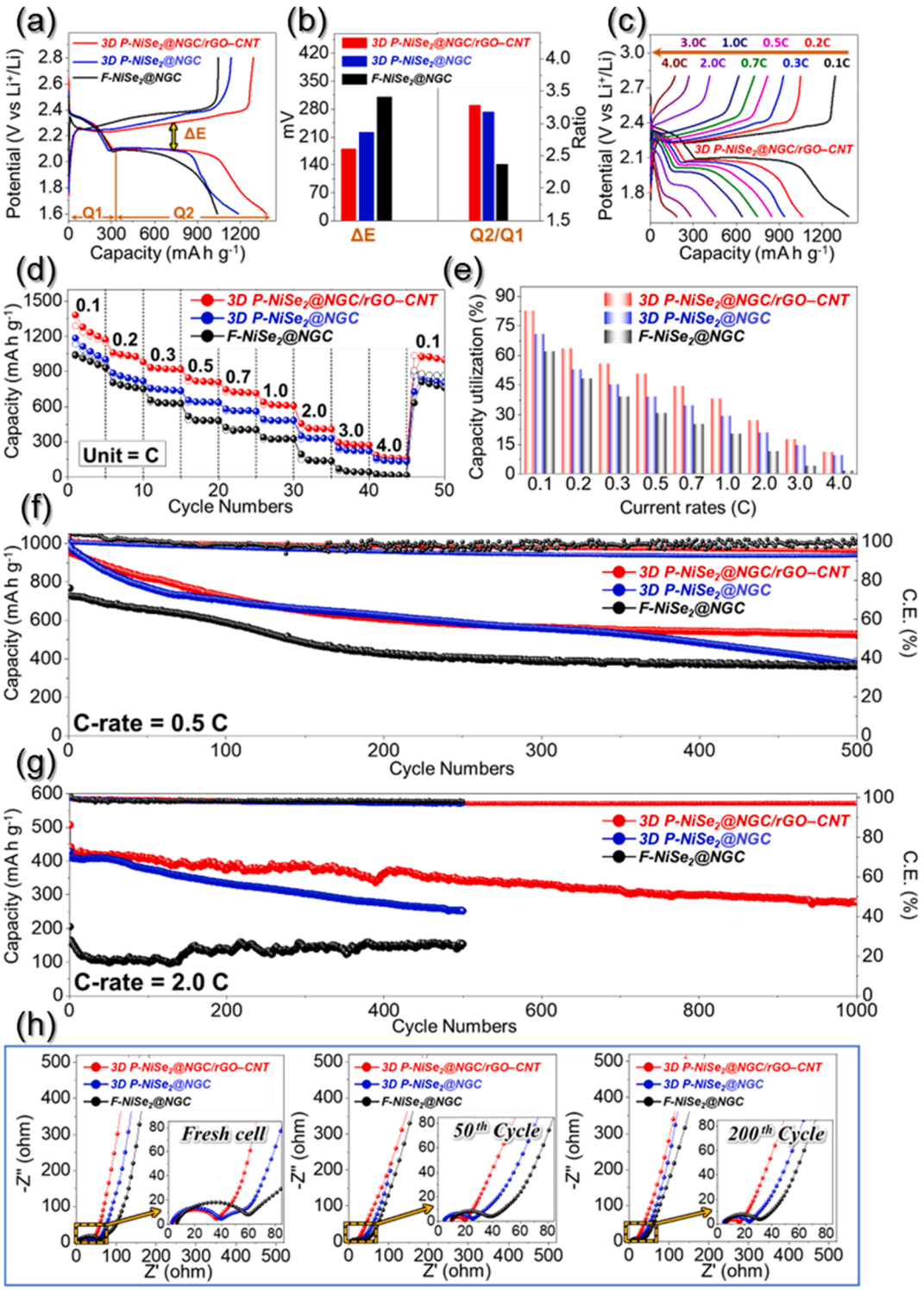

Fig. 6. (a) GCD voltage profiles of different coated separator arrangements at 0.1C, (b) ΔE and Q2/Q1comparison for different coated separator, (c) GCD profiles at various C-rates for Li–S cell featuring 3D P-$NiSe_2$@NGC/rGO–CNT-coated separator, (d) Rate capability tests from 0.1 to 4.0C, (e) Capacity utilization at various C-rates, (f) Cycling performance at 0.5C, (g) Cycling performance at 2.0C, and (h) EIS comparison at different cycling number.

trapped polysulfide species. The cell with a 3D P-$NiSe_2$@NGC/rGO–CNT-coated separator exhibited the highest Q2/Q1 (3.28) compared to the 3D P-$NiSe_2$@NGC (Q2/Q1 = 3.18) and F-$NiSe_2$@NGC (Q2/Q1 = 2.37). This suggested a better electrocatalytic activity of 3D P-$NiSe_2$@NGC/rGO–CNT microspheres towards lithium polysulfide species than the other two cells. However, the values were slightly higher than the theoretical ones due to excess capacity (Q2) from the $LiNO_3$ reduction below 1.7 V during the initial cycle. Correspondingly, the cells with 3D P-$NiSe_2$@NGC/rGO–CNT, 3D P-$NiSe_2$@NGC, and F-$NiSe_2$@NGC-coated separators showed an initial discharge capacity of 1383 (82.5% of theoretical value), 1186 (70.8% of theoretical value), and 1039 (60.0% of theoretical value) mA h g^{-1}, respectively. The highest discharge capacity value for the 3D P-$NiSe_2$@NGC/rGO–CNT-coated separator was clear evidence of kinetically-favored reactions

derived from the conductive, porous, and polar framework that eventually gave rise to high active-material utilization.

The GCD voltage profiles of Li–S cells utilizing different coating arrangements at various C-rates ranging from 0.1 to 4.0C are presented in Fig. 6c and Fig. S10. The cell with 3D P-$NiSe_2$@NGC/rGO–CNT (Fig. 6c) and 3D P-$NiSe_2$@NGC (Fig. S10a) coated separators exhibited well distinguished charge–discharge voltage plateaus even at a high C-rate of 4.0C. However, the difference in voltage plateau lengths resulted in high discharge capacity values for the 3D P-$NiSe_2$@NGC/rGO–CNT-coated separator cell at all C-rates, as shown in Fig. 6d. For instance, an initial discharge capacity of 1383, 1062, 936, 848, 748, 640, 456, 295, and 185 mA h g^{-1} were obtained at 0.1, 0.2, 0.3, 0.5, 0.7, 1.0, 2.0, 3.0, and 4.0C, respectively, for the 3D P-$NiSe_2$@NGC/rGO–CNT-coated separator cell compared to 1186, 887, 759, 656, 580, 492, 351, 246, and 156 mA h g^{-1}, respectively, at identical C-rates for the 3D P-$NiSe_2$@NGC-coated separator cell. In contrast, the cell with the F-$NiSe_2$@NGC-coated separator exhibited low discharge-capacity values of 1039, 808, 656, 518, 423, 338, 194, 69, and 25 mA h g^{-1} at 0.1, 0.2, 0.3, 0.5, 0.7, 1.0, 2.0, 3.0, and 4.0C, respectively. When the current was reversed to 0.1C, the recovered specific discharge capacity corresponding to the 3D P-$NiSe_2$@NGC/rGO–CNT coated separator (1000 mA h g^{-1}) was higher than those of 3D P-$NiSe_2$@NGC (804 mA h g^{-1}) and F-$NiSe_2$@NGC (762 mA h g^{-1}) coated separator interlayers, indicating high reversibility of the redox processes. Furthermore, the capacity utilization values were calculated at different C-rates for various coated separator arrangements and summarized in Fig. 6e. Generally, capacity utilization is a direct measurement of the amount of active material consumed during the redox reaction. As predicted, the 3D P-$NiSe_2$@NGC/rGO–CNT-coated separator cell exhibited the highest capacity utilization values among all the cells. The high active-material utilization is consistent with the CV results, which predicted the lowest voltage hysteresis and superior electrocatalytic conversion capability for the 3D P-$NiSe_2$@NGC/rGO–CNT microspheres.

The assembled cells were further assessed with cycling performance at low (0.5C) and high (2.0C) C-rates. Fig. 6f shows the cycling performance of the assembled cells with different coating separator arrangements at 0.5C for 500 cycles. The cell with 3D P-$NiSe_2$@NGC/rGO–CNT-coated separator exhibited an initial discharge capacity of 953 mA h g^{-1} compared to the 3D P-$NiSe_2$@NGC (989 mA h g^{-1}), and F-$NiSe_2$@NGC (767 mA h g^{-1}) coated separators. Although after 500 cycles, 55.2% of the initial capacity was retained for the 3D P-$NiSe_2$@NGC/rGO–CNT-coated separator (526 mA h g^{-1}). In contrast, the 3D P-$NiSe_2$@NGC and F-$NiSe_2$@NGC-coated separator retained 37.8% (374 mA h g^{-1}) and 47.1% (362 mA h g^{-1}), respectively, of the initial capacity. In addition, the average capacity decay rate per cycle is lowest for the 3D P-$NiSe_2$@NGC/rGO–CNT-coated separator (0.08%) compared to the 3D P-$NiSe_2$@NGC (0.12%) and F-$NiSe_2$@NGC (0.10%) coated separators. The low-capacity decay rate for the F-$NiSe_2$@NGC-coated separator was due to the availability of higher surface chemisorption sites compared to those for the 3D P-$NiSe_2$@NGC. Moreover, the high Coulombic efficiency values throughout the cycling suggested highly reversible redox processes inside the cell. The high-capacity retention values for 3D P-$NiSe_2$@NGC/rGO–CNT microspheres confirmed the efficient LiPS anchoring within the cathodic domain, thus minimizing active material loss during prolonged cycling. Similar trends were observed for the cycling performance of all the assembled cells at a high C-rate of 2.0C, as shown in Fig. 6g. An initial discharge capacity of 507, 428, and 205 mA h g^{-1} was obtained for the 3D P-$NiSe_2$@NGC/rGO–CNT, 3D P-$NiSe_2$@NGC, and F-$NiSe_2$@NGC-coated separators, respectively. However, after 1000 cycles, 54.8% of the initial capacity was retained for the 3D P-$NiSe_2$@NGC/rGO–CNT-coated separator (278 mA h g^{-1}) with an average capacity decay rate of just 0.04% per cycle. In contrast, the 3D P-$NiSe_2$@NGC and F-$NiSe_2$@NGC-coated separators exhibited much lower capacity values throughout the cycling. The prolonged cycling stability is consistent with the conclusion that the observed nanostructure advantages in 3D P-$NiSe_2$@NGC/rGO–CNT microspheres facilitated an effective polysulfide species capture and suppressed active material loss. The improved redox kinetics facilitated a smooth diffusion of charged species during electrochemical processes and the effective absorption of undesired volume fluctuations due to the highly conductive and porous framework.

We employed electrochemical impedance spectroscopy (EIS) to better understand the enhancement in the electrochemical performance and redox kinetics within the prepared nanostructures. Fig. 6h shows the Nyquist plots obtained at different cycle numbers during cycling at a C-rate of 2.0C in the charge state. The equivalent circuit fitting of the Nyquist plots for Li–S cells utilizing various coated separators is shown in Fig. S11. The EIS for fresh cells exhibited a depressed semicircle in the high-frequency region. The first intercept of the semicircle on the *x*-axis corresponds to the solution or electrolyte resistance (R_e). In contrast, the second intercept represents the charge-transfer resistance (R_{ct}) followed by an inclined line in the low-frequency region associated with Li^+-ion diffusion [66]. The cell with a 3D P-$NiSe_2$@NGC/rGO–CNT-coated separator exhibited the lowest R_{ct} (~33 Ω) compared to the 3D P-$NiSe_2$@NGC (~36 Ω) and F-$NiSe_2$@NGC (~53 Ω) cells. Even during cycling (after the 50th and 200th cycle), the R_{ct} values remained lowest for the 3D P-$NiSe_2$@NGC/rGO–CNT-coated separator cell mainly due to better electrolyte penetration resulting in smooth diffusion of charged species. For instance, at the end of the 200th cycle, the 3D P-$NiSe_2$@NGC/rGO–CNT-coated separator still exhibited low R_{ct} (~10 Ω) compared to 3D P-$NiSe_2$@NGC (~19 Ω) and F-$NiSe_2$@NGC (~26 Ω). The lower R_{ct} values strongly indicated favorable redox kinetics that promoted faster electrocatalytic conversion of polysulfides during the electrochemical processes. The electrochemical performance of the Li–S cell involving the pristine separator is presented in Fig. S12, along with the corresponding discussion.

The 3D P-$NiSe_2$@NGC/rGO–CNT-coated separator as a multifunctional cathodic interlayer was further evaluated with more practical cell parameters, i.e., extremely high effective S-content (73 and 74%), high active material loading (3.7 and 4.5 mg cm^{-2}), and lean E/S ratio (7.0 and 5.7 μL mg^{-1}). The obtained electrochemical results are presented in Fig. 7. The Li–S cell with a high-loading S-electrode (3.7 mg cm^{-2}) displayed considerable rate capability performance (Fig. 7a). The cell exhibited a discharge capacity of 802, 646, 600, 461, and 393 mA h g^{-1} at a C-rate of 0.1, 0.15, 0.2. 0.25, and 0.3C, respectively. When the current was reversed, the cell recovered the initial capacity values at 0.1C. The GCD voltage profiles in Fig. 7b indicated that the typical voltage plateaus involving two-step sulfur redox reactions remained intact. The cells were further subjected to the cycling performance at 0.1C, as shown in Fig. 7c. For active material loading and E/S values of 3.7 mg cm^{-2} and 7.0 μL mg^{-1}, respectively, the cell exhibited an initial discharge capacity of 755 mA h g^{-1} which steadily increased to 880 mA h g^{-1} for the first few cycles mainly due to an activation process, which is commonly observed in high loading electrodes [15]. After 400 continuous cycles, a discharge capacity of 562 mA h g^{-1} (74% retention) was still obtained with an average capacity decay rate of just 0.06%. Similar trends were observed when the sulfur loading and E/S values changed to 4.5 mg cm^{-2} and 5.7 μL mg^{-1}, respectively. The cell exhibited a discharge capacity of 416 mA h g^{-1} after 400 continuous cycles, indicating an average capacity decay rate of 0.10%. The above electrochemical results suggested that the cell parameters were relatively more feasible and indicated extremely stable sulfur redox processes primarily due to the robust nanostructures of the 3D P-$NiSe_2$@NGC/rGO–CNT microspheres. Fig. 7d and Table S2 summarize the electrochemical performance obtained in previous works based on various practical parameters and compare them with the present work. As observed in Fig. 7d, the cell performance was superior or comparable to that observed in the previous studies, especially considering the high effective S-content and low E/S ratio. This again proved that the structural advantages in 3D P-$NiSe_2$@NGC/rGO–CNT microspheres enhanced the efficient immobilization of active material in the cathodic region and promoted an efficient electrocatalytic conversion. Our results

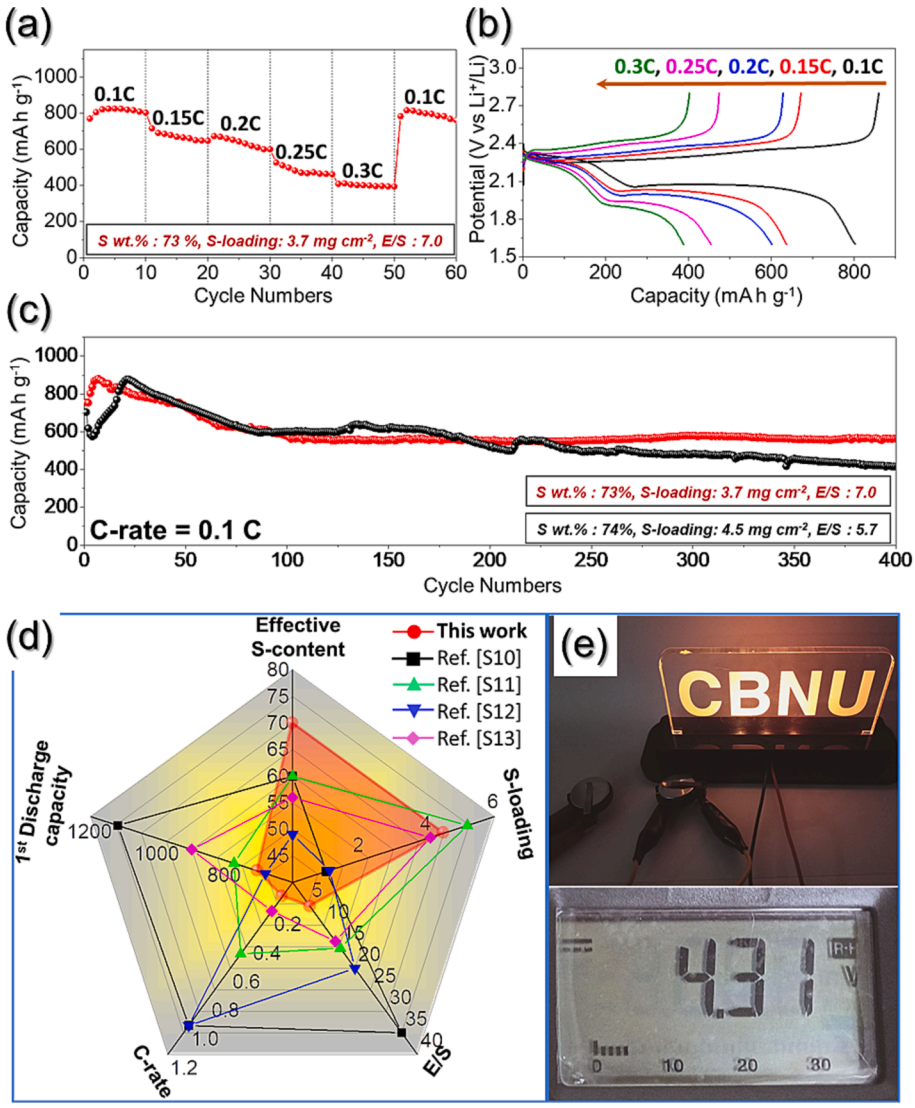

Fig. 7. (a) Rate capability results of Li–S featuring high-loading electrodes and 3D P-$NiSe_2$@NGC/rGO–CNT-coated separator, (b) Respective GCD voltage profiles at various C-rates ranging from 0.1 to 0.3C, (c) Cycling performance with different cell parameters at 0.1C, (d) Comparison of the electrochemical performance obtained in this work to the previous reports, and (e) Digital image of a light-emitting diode (5 V, 10 mW) powered by two cells utilized after cycling-performance tests at 0.1C.

thus demonstrated that the rational engineering strategy presented in this study could be adopted for more practical applications of LSBs even under severe battery parameters. To verify the above results, we measured the performance of the cycled cells (Fig. 7c) as a power source for a light-emitting diode (10 mW, 5 V). As Fig. 7e shows, the series cell combination provided uninterrupted power to the load for 0.5 h and thus established the viability of cycled cells for practical applications.

2.3. *Post-cycling characterizations of the cycled Li–S cells*

Finally, the cells with different coated separators were disassembled after cycling at 2.0C, and their respective sulfur electrodes and coated separators were carefully removed and analyzed. The FE-SEM micrographs of the cycled 3D P-$NiSe_2$@NGC/rGO–CNT-coated separator in Fig. 8a and 8b show that the spherical and porous morphology of the nanostructure remained intact primarily due to the self-supporting rGO–CNT framework that maintained the structural robustness even after prolonged cycling (1000cycles). Also, no sign of polysulfide agglomeration over the spherical surface was observed, indicating an effective electrocatalytic conversion of trapped LiPS species. These observations agreed well with the FE-SEM image in Fig. 8g of the cycled sulfur electrode paired with the 3D P-$NiSe_2$@NGC/rGO–CNT-coated separator, which exhibited particle-type morphology with no sedimentation of any foreign species. This observation was also apparent from the digital image of the separator that showed a transparent color (Fig. 8a inset). In contrast, the FE-SEM micrographs of the 3D P-$NiSe_2$@NGC (Fig. 8c and 8d) coated separator suggested polysulfide agglomeration over the microsphere surface with a slightly ruptured morphology due to the microsphere's lower structural integrity or robustness. The slightly yellowish color of the separator (Fig. 8c inset) further confirmed the FE-SEM results. Finally, the FE-SEM micrographs of the cycled F-$NiSe_2$@NGC (Fig. 8e and 8f) coated separator indicated high deposits of LiPS along with the complete destruction of the spherical morphology. The pale-yellow color of the separator (inset) further verifies the same. Additionally, the FE-SEM images of the cycled sulfur electrode paired with 3D P-$NiSe_2$@NGC (Fig. 8h) and F-$NiSe_2$@NGC (Fig. 8i) coated separators displayed significant polysulfide accumulation, indicating that the structure was not stable enough to endure prolonged cycling effects. The post-cycling results again support the conclusion that the structural integrity in the 3D P-$NiSe_2$@NGC/rGO–CNT microsphere enhanced high active-material utilization and reduced parasitic polysulfide migration effect towards the Li-anode. The

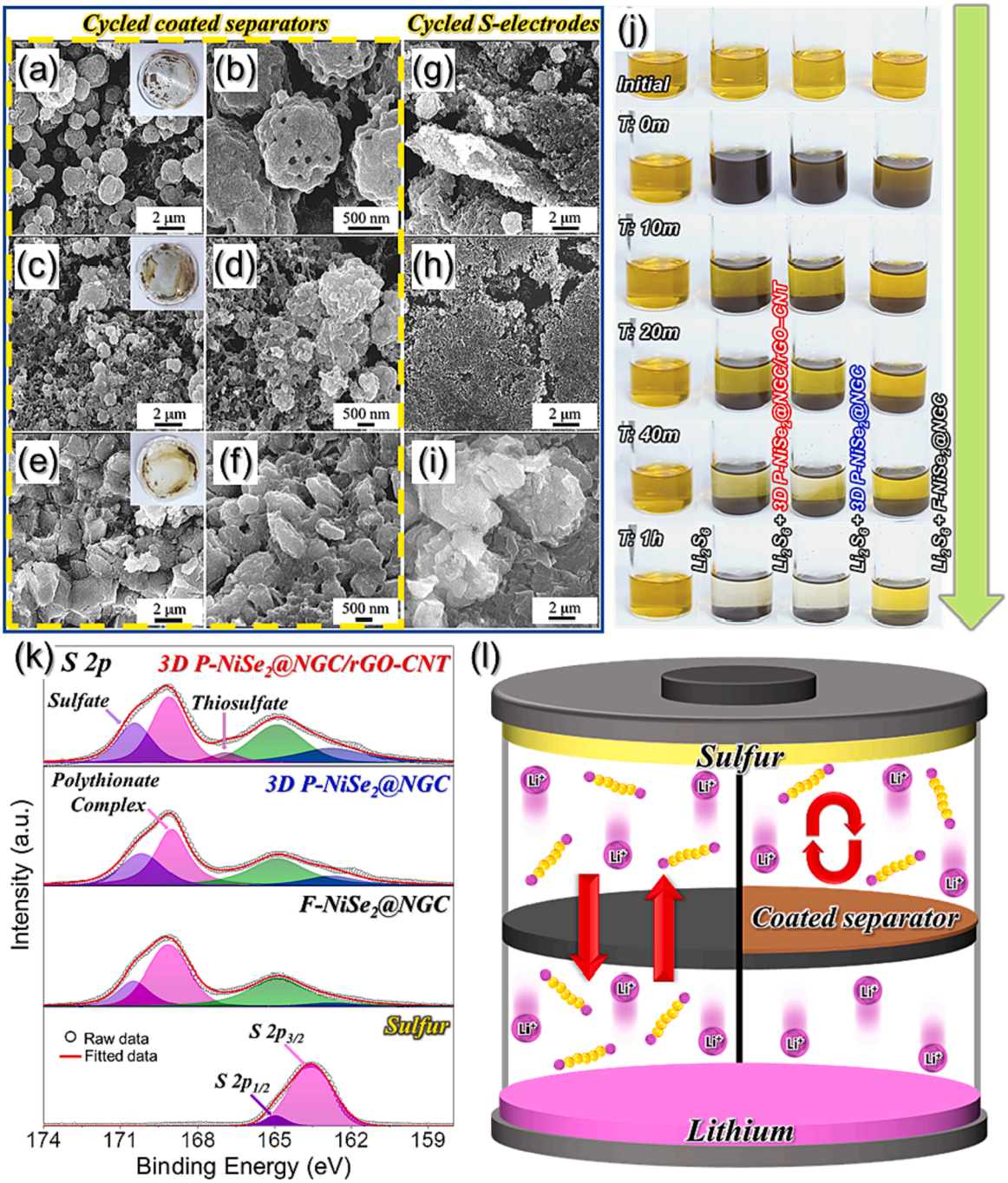

Fig. 8. Post-cycling characterizations of the Li–S cells utilizing various coated separators: (a, b) FE-SEM micrographs of the 3D P-$NiSe_2$@NGC/rGO–CNT, (c, d) 3D P-$NiSe_2$@NGC, (e, f) F-$NiSe_2$@NGC coated separators after cycling at 2.0C, (g) FE-SEM micrographs of the cycled S-electrode paired with 3D P-$NiSe_2$@NGC/rGO–CNT, (h) 3D P-$NiSe_2$@NGC, and (i) F-$NiSe_2$@NGC coated separators, (j) Digital images of the polysulfide adsorption tests at different interval, (k) S 2*p* XPS spectra of the powders collected from the cycled coated separators, and (l) Schematic illustration of the polysulfide anchoring mechanism over the surface of coated separators.

digital images of the visual demonstration of polysulfide adsorption tests in Fig. 8j also verified the abovementioned results. The accompanying color change of the polysulfide solution from pale yellow to substantially clear (after T = 1 h) for the 3D P-$NiSe_2$@NGC/rGO–CNT sample implied an effective trapping of polysulfide species by the polar $NiSe_2$ nanocrystals. Fig. 8k shows the XPS spectrum of the powders collected from the cycled coated separator and analyzed for the S 2*p* photoelectron signal. The S 2*p* spectrum for elemental sulfur was also obtained for comparison. The S 2*p* signal for the cycled 3D P-$NiSe_2$@NGC/rGO–CNT sample exhibited three prominent well-fitted peaks at 166.9, 168.1, and 170.4 eV corresponding to the thiosulfate ($-S_2O_3^{2-}$), polythionate complexes, and the sulfate ($-SO_4^{2-}$) groups, respectively [25]. A thiosulfate peak usually indicated an interaction between the polysulfide species and $NiSe_2$ nanocrystals that allowed an efficient anchoring of higher-order soluble LiPS and their electrocatalytic conversion to lower-order insoluble polysulfides. Likewise, the appearance of a peak corresponding to the polythionate complexes explained the reaction between elemental sulfur and nucleophilic species such as HS^- or SO_3^{2-}, which probably suppressed the polysulfide crossover. The decomposition of LiTFSI salt during the redox processes was considered a prime source of Li_xSO_y species that resulted in a peak ascribed to the sulfate ($-SO_4^{2-}$) species. In contrast, the thiosulfate peak intensity was exceptionally low

for the cycled 3D P-$NiSe_2$@NGC and F-$NiSe_2$@NGC samples, suggesting poor electrocatalytic conversion over extended cycling. These results again confirmed the considerable capability of the 3D P-$NiSe_2$@NGC/rGO–CNT microspheres to suppress polysulfide diffusion and alleviate active material loss, thus enhancing their overall electrochemical performance. A schematic presentation involving the working mechanism of the multifunctional cathodic interlayer is illustrated in Fig. 8l.

Overall, the pairing of a rationally designed nanostructure comprising a highly conductive, porous, and structurally stable framework as a cathodic interlayer resulted in an overall improvement in the cell performance purely due to the high utilization of active material and kinetically favored redox kinetics.

3. Conclusions

In summary, we proposed and utilized a rationally engineered 3D nanostructure (P-$NiSe_2$@NGC/rGO–CNT microspheres) as a multifunctional cathodic interlayer to improve the overall Li–S performance. The spray-pyrolysis-assisted microspheres comprised highly conductive rGO–CNT framework that supported fast charge transfer (in the form of primary and secondary transport pathways for electrons), PS nanobeads-derived macropores that ensured smooth diffusion of charged species by lowering the effective diffusion length, and well-embedded $NiSe_2$-core@NGC shell nanocrystals that behaved as active chemisorption sites for the efficient trapping and electrocatalytic conversion of polysulfide species. The interlayer served as "polysulfide sieves" for efficiently suppressing the polysulfide crossover and improving the sulfur redox kinetics. Accordingly, the Li–S with the regular sulfur electrode and 3D P-$NiSe_2$@NGC/rGO–CNT-coated separator interlayer exhibited significantly high rate capability (till 4.0C) and stable cycling performance (1000 cycles at 2.0C with an average capacity decay rate of just 0.04% per cycle). Even with more severe cell parameters (sulfur content = 74%, sulfur-loading = 4.5 mg cm^{-2}, and E/S = 5.7 μL mg^{-1}), the cell displayed high cycling stability (400 cycles at 0.1C with an average capacity decay rate of just 0.10% per cycle) and feasible rate performance (till 0.3C). Thus, the structural and electrochemical advantages of the systems designed and fabricated in this study provide valuable insights into the design and synthesis of structurally stable nanostructures, especially for metal-sulfur battery applications.

CRediT authorship contribution statement

Rakesh Saroha: . **Hyun Ho Choi:** . **Jung Sang Cho:** Supervision, Writing – review & editing.

Declaration of Competing Interest

The authors declare that they have no known competing financial interests or personal relationships that could have appeared to influence the work reported in this paper.

Data availability

No data was used for the research described in the article.

Acknowledgments

This work was supported by the National Research Foundation of Korea (NRF), funded by the Korean government (MSIP) [grant numbers NRF-2021R1A4A2001687 and NRF-2021R1I1A3057700]. This work was also supported by the National Research Foundation of Korea(NRF) grant funded by the Korea government (MSIT) [No. RS-2023-00217581].

Appendix A. Supplementary data

Supplementary data to this article can be found online at https://doi.org/10.1016/j.cej.2023.145391.

References

[1] M.-S. Balogun, H. Yang, Y. Luo, W. Qiu, Y. Huang, Z.-Q. Liu, Y. Tong, Achieving high gravimetric energy density for flexible lithium-ion batteries facilitated by core–double-shell electrodes, Energ. Environ. Sci. 11 (2018) 1859–1869.
[2] R. Saroha, A.K. Panwar, Y. Sharma, P.K. Tyagi, S. Ghosh, Development of surface functionalized ZnO-doped $LiFePO_4$/C composites as alternative cathode material for lithium ion batteries, Appl. Surf. Sci. 394 (2017) 25–36, https://doi.org/10.1016/j.apsusc.2016.09.105.
[3] M.E. Sotomayor, C. de La Torre-Gamarra, B. Levenfeld, J.-Y. Sanchez, A. Varez, G.-T. Kim, A. Varzi, S. Passerini, Ultra-thick battery electrodes for high gravimetric and volumetric energy density Li-ion batteries, J. Power Sources 437 (2019), 226923, https://doi.org/10.1016/j.jpowsour.2019.226923.
[4] R. Saroha, A. Gupta, A.K. Panwar, Electrochemical performances of Li-rich layered-layered Li_2MnO_3-$LiMnO_2$ solid solutions as cathode material for lithium-ion batteries, J. Alloy. Compd. 696 (2017) 580–589, https://doi.org/10.1016/j.jallcom.2016.11.199.
[5] R. Saroha, J.S. Cho, J.-H. Ahn, Synergetic effects of cation (K+) and anion (S2−)-doping on the structural integrity of Li/Mn-rich layered cathode material with considerable cyclability and high-rate capability for Li-ion batteries, Electrochim. Acta 366 (2021), 137471, https://doi.org/10.1016/j.electacta.2020.137471.
[6] Z. Wang, H. Che, W. Lu, Y. Chao, L. Wang, B. Liang, J. Liu, Q. Xu, X. Cui, Application of inorganic quantum dots in advanced lithium–sulfur batteries, Adv. Sci. 10 (2023) 2301355, https://doi.org/10.1002/advs.202301355.
[7] B.D. McCloskey, Attainable gravimetric and volumetric energy density of Li–S and Li ion battery cells with solid separator-protected Li metal anodes, J. Phys. Chem. Lett. 6 (2015) 4581–4588, https://doi.org/10.1021/acs.jpclett.5b01814.
[8] R. Saroha, J.-H. Ahn, J.S. Cho, A short review on dissolved lithium polysulfide catholytes for advanced lithium-sulfur batteries, Korean J. Chem. Eng. 38 (2021) 461–474, https://doi.org/10.1007/s11814-020-0729-5.
[9] A. Chen, W. Liu, H. Hu, T. Chen, B. Ling, K. Liu, Three-dimensional TiO_2-B nanotubes/carbon nanotubes intertwined network as sulfur hosts for high performance lithium−sulfur batteries, J. Power Sources 400 (2018) 23–30, https://doi.org/10.1016/j.jpowsour.2018.08.004.
[10] R. Saroha, J.H. Oh, Y.H. Seon, Y.C. Kang, J.S. Lee, D.W. Jeong, J.S. Cho, Freestanding interlayers for Li-S batteries: Design and synthesis of hierarchically porous N-doped C nanofibers comprising vanadium nitride quantum dots and MOF-derived hollow N-doped C nanocages, J. Mater. Chem. A 9 (19) (2021) 11651–11664.
[11] Z. Liang, J. Shen, X. Xu, F. Li, J. Liu, B. Yuan, Y. Yu, M. Zhu, Advances in the development of single-atom catalysts for high-energy-density lithium–sulfur batteries, Adv. Mater. 34 (2022) 2200102, https://doi.org/10.1002/adma.202200102.
[12] X. Li, K. Ding, B. Gao, Q. Li, Y. Li, J. Fu, X. Zhang, P.K. Chu, K. Huo, Freestanding carbon encapsulated mesoporous vanadium nitride nanowires enable highly stable sulfur cathodes for lithium-sulfur batteries, Nano Energy 40 (2017) 655–662, https://doi.org/10.1016/j.nanoen.2017.09.018.
[13] R. Saroha, J.H. Oh, J.S. Lee, Y.C. Kang, S.M. Jeong, D.-W. Kang, C. Cho, J.S. Cho, Hierarchically porous nanofibers comprising multiple core–shell Co_3O_4@graphitic carbon nanoparticles grafted within N-doped CNTs as functional interlayers for excellent Li–S batteries, Chem. Eng. J. 426 (2021), 130805, https://doi.org/10.1016/j.cej.2021.130805.
[14] Z.A. Ghazi, X. He, A.M. Khattak, N.A. Khan, B. Liang, A. Iqbal, J. Wang, H. Sin, L. Li, Z. Tang, MoS2/celgard separator as efficient polysulfide barrier for long-life lithium–sulfur batteries, Adv. Mater. 29 (2017) 1606817, https://doi.org/10.1002/adma.201606817.
[15] R. Saroha, J.S. Cho, Nanofibers comprising interconnected chain-like hollow N-doped C nanocages as 3D free-standing cathodes for Li–S batteries with super-high sulfur content and lean electrolyte/sulfur ratio, Small Methods 6 (2022) 2200049, https://doi.org/10.1002/smtd.202200049.
[16] J. Shen, X. Xu, J. Liu, Z. Wang, S. Zuo, Z. Liu, D. Zhang, J. Liu, M. Zhu, Unraveling the catalytic activity of Fe–based compounds toward Li_2S_x in Li–S chemical system from d–p bands, Adv. Energy Mater. 11 (2021) 2100673, https://doi.org/10.1002/aenm.202100673.
[17] Z. Wang, J. Shen, X. Xu, J. Yuan, S. Zuo, Z. Liu, D. Zhang, J. Liu, In-situ synthesis of carbon-encapsulated atomic cobalt as highly efficient polysulfide electrocatalysts for highly stable lithium–sulfur batteries, Small 18 (2022) 2106640, https://doi.org/10.1002/smll.2021006640.
[18] P. Chiochan, S. Kaewruang, N. Phattharasupakun, J. Wutthiprom, T. Maihom, J. Limtrakul, S.S. Nagarkar, S. Horike, M. Sawangphruk, Chemical adsorption and physical confinement of polysulfides with the janus-faced interlayer for high-performance lithium-sulfur batteries, Sci. Rep. 7 (2017) 1–10, https://doi.org/10.1038/s41598-017-18108-0.
[19] Y.H. Seon, R. Saroha, J.S. Cho, Hierarchically porous N-doped C nanofibers comprising TiO_2 quantum dots and ZiF-8-derived hollow C nanocages as ultralight interlayer for stable Li–S batteries, Compos. B Eng. 237 (2022), 109856, https://doi.org/10.1016/j.compositesb.2022.109856.
[20] M. Tian, F. Pei, M. Yao, Z. Fu, L. Lin, G. Wu, G. Xu, H. Kitagawa, X. Fang, Ultrathin MOF nanosheet assembled highly oriented microporous membrane as an interlayer

for lithium-sulfur batteries, Energy Storage Mater. 21 (2018) 14–21, https://doi.org/10.1016/j.ensm.2018.12.016.
[21] R. Saroha, Y.H. Seon, B. Jin, Y.C. Kang, D.-W. Kang, S.M. Jeong, J.S. Cho, Self-supported hierarchically porous 3D carbon nanofiber network comprising Ni/Co/$NiCo_2O_4$ nanocrystals and hollow N-doped C nanocages as sulfur host for highly reversible Li–S batteries, Chem. Eng. J. 446 (2022), 137141, https://doi.org/10.1016/j.cej.2022.137141.
[22] Y.X. Yao, X.Q. Zhang, B.Q. Li, C. Yan, P.Y. Chen, J.Q. Huang, Q. Zhang, A compact inorganic layer for robust anode protection in lithium-sulfur batteries, InfoMat. 2 (2020) 379–388, https://doi.org/10.1002/inf2.12046.
[23] R. Saroha, H.S. Ka, J.S. Cho, A novel three-dimensional ordered mesoporous microspheres comprising N-doped graphitic carbon-coated Fe_xP nanoparticles as multifunctional interlayers to suppress polysulfide crossover in Li–S batteries, Appl. Surf. Sci. 612 (2022), 155892, https://doi.org/10.1016/j.apsusc.2022.155892.
[24] X.-B. Cheng, J.-Q. Huang, Q. Zhang, Li metal anode in working lithium-sulfur batteries, J. Electrochem. Soc. 165 (2017) A6058, https://doi.org/10.1149/2.0111801jes.
[25] J.M. Choi, R. Saroha, J.S. Kim, M.R. Jang, J.S. Cho, Porous nanofibers comprising VN nanodots and densified N-doped CNTs as redox-active interlayers for Li–S batteries, J. Power Sources 559 (2023), 232632, https://doi.org/10.1016/j.jpowsour.2023.232632.
[26] J. Scheers, S. Fantini, P. Johansson, A review of electrolytes for lithium–sulphur batteries, J. Power Sources 255 (2014) 204–218, https://doi.org/10.1016/j.jpowsour.2014.01.023.
[27] H.-L. Wu, M. Shin, Y.-M. Liu, K.A. See, A.A. Gewirth, Thiol-based electrolyte additives for high-performance lithium-sulfur batteries, Nano Energy 32 (2017) 50–58, https://doi.org/10.1016/j.nanoen.2016.12.015.
[28] L. Fan, M. Li, X. Li, W. Xiao, Z. Chen, J. Lu, Interlayer material selection for lithium-sulfur batteries, Joule 3 (2019) 361–386, https://doi.org/10.1016/j.joule.2019.01.003.
[29] R. Saroha, J. Heo, X. Li, N. Angulakshmi, Y. Lee, H.-J. Ahn, J.-H. Ahn, J.-H. Kim, Asymmetric separator integrated with ferroelectric-$BaTiO_3$ and mesoporous-CNT for the reutilization of soluble polysulfide in lithium-sulfur batteries, J. Alloy. Compd. 893 (2022), 162272, https://doi.org/10.1016/j.jallcom.2021.162272.
[30] X. Liang, C. Hart, Q. Pang, A. Garsuch, T. Weiss, L.F. Nazar, A highly efficient polysulfide mediator for lithium–sulfur batteries, Nat. Commun. 6 (2015) 1–8, https://doi.org/10.1038/ncomms6682.
[31] R. Saroha, J. Heo, Y. Liu, N. Angulakshmi, Y. Lee, K.-K. Cho, H.-J. Ahn, J.-H. Ahn, V_2O_3-decorated carbon nanofibers as a robust interlayer for long-lived, high-performance, room-temperature sodium–sulfur batteries, Chem. Eng. J. 431 (2022), 134205, https://doi.org/10.1016/j.cej.2021.134205.
[32] Z. Jian, H. Li, R. Cao, H. Zhou, H. Xu, G. Zhao, Y. Xing, S. Zhang, Polydopamine-coated hierarchical tower-shaped carbon for high-performance lithium-sulfur batteries, Electrochim. Acta 319 (2019) 359–365, https://doi.org/10.1016/j.electacta.2019.06.145.
[33] J. Wang, L. Lu, D. Shi, R. Tandiono, Z. Wang, K. Konstantinov, H. Liu, A conductive polypyrrole-coated, sulfur–carbon nanotube composite for use in lithium–sulfur batteries, ChemPlusChem 78 (2013) 318–324, https://doi.org/10.1002/cplu.201200293.
[34] L. Borchardt, M. Oschatz, S. Kaskel, Carbon materials for lithium sulfur batteries—ten critical questions, Chem. Eur. J. 22 (2016) 7324–7351, https://doi.org/10.1002/chem.201600040.
[35] P. Chiochan, S. Kosasang, N. Ma, S. Duangdangchote, P. Suktha, M. Sawangphruk, Confining Li_2S_6 catholyte in 3D graphene sponge with ultrahigh total pore volume and oxygen-containing groups for lithium-sulfur batteries, Carbon 158 (2020) 244–255, https://doi.org/10.1016/j.carbon.2019.12.015.
[36] J. He, A. Bhargav, H. Yaghoobnejad Asl, Y. Chen, A. Manthiram, 1T′-ReS2 nanosheets in situ grown on carbon nanotubes as a highly efficient polysulfide electrocatalyst for stable Li–S batteries, Adv. Energy Mater. 10 (2020) 2001017, https://doi.org/10.1002/aenm.202001017.
[37] J. Park, B.C. Yu, J.S. Park, J.W. Choi, C. Kim, Y.E. Sung, J.B. Goodenough, Tungsten disulfide catalysts supported on a carbon cloth interlayer for high performance Li–S battery, Adv. Energy Mater. 7 (2017) 1602567, https://doi.org/10.1002/aenm.201602567.
[38] X.-X. Zheng, S.-X. Zhao, J.-L. Yang, Y.-M. Lu, Q.-L. Wu, X.-T. Zeng, Facile synthesis of porous Co_3O_4 nanoflakes as an interlayer for high performance lithium–sulfur batteries, Dalton Trans. 49 (2020) 5677–5683, https://doi.org/10.1039/D0DT00429D.
[39] W. Li, J. Hicks-Garner, J. Wang, J. Liu, A.F. Gross, E. Sherman, J. Graetz, J.J. Vajo, P. Liu, V_2O_5 polysulfide anion barrier for long-lived Li–S batteries, Chem. Mater. 26 (2014) 3403–3410, https://doi.org/10.1021/cm500575q.
[40] R. Liu, F. Guo, X. Zhang, J. Yang, M. Li, W. Miaomiao, H. Liu, M. Feng, L. Zhang, Novel "bird-nest" structured Co3O4/acidified multiwall carbon nanotube (ACNT) hosting materials for lithium–sulfur batteries, ACS Appl. Energy Mater. 2 (2019) 1348–1356, https://doi.org/10.1021/acsaem.8b01914.
[41] H. Yuan, X. Chen, G. Zhou, W. Zhang, J. Luo, H. Huang, Y. Gan, C. Liang, Y. Xia, J. Zhang, J. Wang, X. Tao, Efficient activation of Li_2S by transition metal phosphides nanoparticles for highly stable lithium–sulfur batteries, ACS Energy Lett. 2 (7) (2017) 1711–1719.
[42] C. Deng, Z. Wang, S. Wang, J. Yu, D.J. Martin, A.K. Nanjundan, Y. Yamauchi, Double-layered modified separators as shuttle suppressing interlayers for lithium–sulfur batteries, ACS Appl. Mater. Interfaces 11 (2018) 541–549, https://doi.org/10.1021/acsami.8b14196.
[43] S.-H. Chung, C.-H. Chang, A. Manthiram, A carbon-cotton cathode with ultrahigh-loading capability for statically and dynamically stable lithium–sulfur batteries, ACS Nano 10 (2016) 10462–10470, https://doi.org/10.1021/acsnano.6b06369.
[44] M. Li, D. Yang, J.J. Biendicho, X.u. Han, C. Zhang, K. Liu, J. Diao, J. Li, J. Wang, M. Heggen, R.E. Dunin-Borkowski, J. Wang, G. Henkelman, J.R. Morante, J. Arbiol, S.-L. Chou, A. Cabot, Enhanced polysulfide conversion with highly conductive and electrocatalytic iodine-doped bismuth selenide nanosheets in lithium–sulfur batteries, Adv. Funct. Mater. 32 (26) (2022) 2200529, https://doi.org/10.1002/adfm.202200529.
[45] S.H. Chung, A. Manthiram, Carbonized eggshell membrane as a natural polysulfide reservoir for highly reversible Li-S batteries, Adv. Mater. 26 (2014) 1360–1365, https://doi.org/10.1002/adma.201304365.
[46] L. Jiao, Y. Luo, L. Cheng, Ni_3S_2/$NiSe_2$ hollow spheres with low bonding energy Ni-Se bonds for excellent lithium-ion charge-discharge stability, Colloids Surf. A Physicochem. Eng. Asp. 664 (2023), 131122, https://doi.org/10.1016/j.colsurfa.2023.131122.
[47] H. Wang, N. Deng, S. Wang, X. Wang, Y. Li, Q. Zeng, S. Luo, X. Cui, B. Cheng, W. Kang, Advanced preparation and application of transition metal selenides in lithium-sulfur batteries: A review, J. Mater. Chem. A 10 (2022) 23433–23466, https://doi.org/10.1039/D2TA05576G.
[48] M. Wang, L. Fan, X. Wu, Y. Qiu, B. Guan, Y. Wang, N. Zhang, K. Sun, Metallic $NiSe_2$ nanoarrays towards ultralong life and fast Li_2S oxidation kinetics of Li–S batteries, J. Mater. Chem. A 7 (2019) 15302–15308, https://doi.org/10.1039/C9TA03361K.
[49] J.S. Lee, R. Saroha, S.H. Oh, D.H. Shin, S.M. Jeong, J.K. Kim, J.S. Cho, Rational design of perforated bimetallic (Ni, Mo) sulfides/N-doped graphitic carbon composite microspheres as anode materials for superior Na-ion batteries, Small Methods 5 (2021) 2100195, https://doi.org/10.1002/smtd.202100195.
[50] C.S. Kim, J.S. Lee, R. Saroha, Y.B. Park, Y. Chan Kang, D.-W. Kang, S.M. Jeong, J. S. Cho, Porous nitrogen-doped graphene nanofibers comprising metal organic framework-derived hollow and ultrafine layered double metal oxide nanocrystals as high-performance anodes for lithium-ion batteries, J. Power Sources 523 (2022), 231030, https://doi.org/10.1016/j.jpowsour.2022.231030.
[51] T.-H. Ko, K. Devarayan, M.-K. Seo, H.-Y. Kim, B.-S. Kim, Facile synthesis of core/shell-like $NiCo_2O_4$-decorated MWCNTs and its excellent electrocatalytic activity for methanol oxidation, Sci. Rep. 6 (2016) 1–9, https://doi.org/10.1038/srep20313.
[52] M. Cheng, H. Fan, Y. Song, Y. Cui, R. Wang, Interconnected hierarchical $NiCo_2O_4$ microspheres as high-performance electrode materials for supercapacitors, Dalton Trans. 46 (2017) 9201–9209, https://doi.org/10.1039/C7DT01289F.
[53] J.S. Lee, R. Saroha, J.S. Cho, Porous microspheres comprising $CoSe_2$ nanorods coated with N-doped graphitic C and polydopamine-derived C as anodes for long-lived Na-ion batteries, Nano-Micro Lett. 14 (2022) 1–22, https://doi.org/10.1007/s40820-022-00855-z.
[54] C.S. Kim, R. Saroha, H.H. Choi, J.H. Oh, G.D. Park, D.-W. Kang, J.S. Cho, High-performance cathode promoted by reduced graphene oxide nanofibers with well-defined interconnected meso-/micro pores for rechargeable Li-Se batteries, J. Ind. Eng. Chem. 121 (2023) 489–498, https://doi.org/10.1016/j.jiec.2023.02.004.
[55] Q.-S. Jiang, W. Li, J. Wu, W. Cheng, J. Zhu, Z. Yan, X. Wang, Y. Ju, Electrodeposited cobalt and nickel selenides as high-performance electrocatalytic materials for dye-sensitized solar cells, J. Mater. Sci. Mater. Electron. 30 (2019) 9429–9437, https://doi.org/10.1007/s10854-019-01273-5.
[56] J.S. Lee, M.S. Jo, R. Saroha, D.S. Jung, Y.H. Seon, J.S. Lee, Y.C. Kang, D.-W. Kang, J.S. Cho, Hierarchically Well-Developed Porous Graphene Nanofibers Comprising N-Doped Graphitic C-Coated Cobalt Oxide Hollow Nanospheres As Anodes for High-Rate Li-Ion Batteries, Small 16 (32) (2020) 2002213.
[57] J.S. Lee, R. Saroha, J.H. Oh, C. Cho, B. Jin, D.-W. Kang, J.S. Cho, Camphene-derived hollow and porous nanofibers decorated with hollow NiO nanospheres and graphitic carbon as anodes for efficient lithium-ion storage, J. Ind. Eng. Chem. 114 (2022) 276–287, https://doi.org/10.1016/j.jiec.2022.07.017.
[58] J.S. Lee, H.S. Ka, R. Saroha, Y.C. Kang, D.-W. Kang, J.S. Cho, Three-dimensional hierarchically porous micro sponge-ball comprising anatase TiO_2 nanodots and nitrogen-doped graphitic carbon as anodes for ultra-stable lithium-ion batteries, J. Energy Storage 66 (2023), 107396, https://doi.org/10.1016/j.est.2023.107396.
[59] J.S. Lee, J.-S. Park, K.W. Baek, R. Saroha, S.H. Yang, Y.C. Kang, J.S. Cho, Coral-like porous microspheres comprising polydopamine-derived N-doped C-coated $MoSe_2$ nanosheets composited with graphitic carbon as anodes for high-rate sodium-and potassium-ion batteries, Chem. Eng. J. 456 (2023), 141118, https://doi.org/10.1016/j.cej.2022.141118.
[60] S.H. Oh, S.M. Park, D.-W. Kang, Y.C. Kang, J.S. Cho, Fibrous network of highly integrated carbon nanotubes/MoO_3 composite bundles anchored with MoO_3 nanoplates for superior lithium ion battery anodes, J. Ind. Eng. Chem. 83 (2020) 438–448, https://doi.org/10.1016/j.jiec.2019.12.017.
[61] Y. Yang, Y. Kang, H. Zhao, X. Dai, M. Cui, X. Luan, X. Zhang, F. Nie, Z. Ren, W. Song, An interfacial electron transfer on tetrahedral NiS2/NiSe2 heterocages with dual-phase synergy for efficiently triggering the oxygen evolution reaction, Small 16 (2020) 1905083, https://doi.org/10.1002/smll.201905083.
[62] R. Saroha, A.K. Panwar, Effect of in situ pyrolysis of acetylene (C2H2) gas as a carbon source on the electrochemical performance of LiFePO4 for rechargeable lithium-ion batteries, J. Phys. D Appl. Phys. 50 (25) (2017), 255501, https://doi.org/10.1088/1361-6463/aa708c.
[63] Y. Tian, G. Li, Y. Zhang, D. Luo, X. Wang, Y. Zhao, H. Liu, P. Ji, X. Du, J. Li, Z. Chen, Low-bandgap Se-deficient antimony selenide as a multifunctional polysulfide barrier toward high-performance lithium–sulfur batteries, Adv. Mater. 32 (4) (2020) 1904876.
[64] J. Zhou, R. Li, X. Fan, Y. Chen, R. Han, W. Li, J. Zheng, B. Wang, X. Li, Rational design of a metal–organic framework host for sulfur storage in fast, long-cycle Li–S

batteries, Energ. Environ. Sci. 7 (2014) 2715–2724, https://doi.org/10.1039/C4EE01382D.

[65] H. Zhou, Q. Tang, Q. Xu, Y. Zhang, C. Huang, Y. Xu, A. Hu, X. Chen, Enhanced performance of lithium–sulfur batteries based on single-sided chemical tailoring, and organosiloxane grafted PP separator, RSC Adv. 10 (2020) 18115–18123, https://doi.org/10.1039/D0RA02833A.

[66] R. Saroha, A.K. Panwar, Y. Sharma, Physicochemical and electrochemical performance of LiFe1−xNixPO4 ($0 \leq x \leq 1.0$) solid solution as potential cathode material for rechargeable lithium-ion battery, Ceram. Int. 43 (2017) 5734–5742, https://doi.org/10.1016/j.ceramint.2017.01.115.